JGR Planets

RESEARCH ARTICLE
10.1029/2022JE007422

Special Section:
Fifteen Years of THEMIS Mission

A Comprehensive Model for Pickup Ion Formation at the Moon

A. R. Poppe[1,2], J. S. Halekas[2,3], and Y. Harada[4]

[1]Space Sciences Laboratory, University of California at Berkeley, Berkeley, CA, USA, [2]Solar System Exploration Research Virtual Institute, NASA Ames Research Center, Moffett Field, CA, USA, [3]Department of Physics and Astronomy, University of Iowa, Iowa City, IA, USA, [4]Department of Geophysics, Kyoto University, Kyoto, Japan

Key Points:

- We constructed an observationally based model of 18 neutral and 20 ionized species from the lunar exosphere
- Dominant pickup ion species are H_2^+, He^+, CO^+, $^{40}Ar^+$, Al^+, Na^+, K^+, Si^+, Ca^+, and O^+ with asymmetric spatial distribution
- The model underestimates pickup ion fluxes when compared to ARTEMIS observations, and we suggest CO_2^+ as the missing component

Supporting Information:

Supporting Information may be found in the online version of this article.

Correspondence to:

A. R. Poppe,
poppe@berkeley.edu

Citation:

Poppe, A. R., Halekas, J. S., & Harada, Y. (2022). A comprehensive model for pickup ion formation at the Moon. *Journal of Geophysical Research: Planets*, *127*, e2022JE007422. https://doi.org/10.1029/2022JE007422

Received 6 JUN 2022
Accepted 19 SEP 2022

Abstract The lunar exosphere is an ensemble of multiple overlapping, noninteracting neutral distributions that reflect the primary physical processes acting on the lunar surface. While previous observations have detected and constrained the behavior of some species, many others have only circumstantial evidence or theoretical modeling suggesting their presence. Many species are so tenuous as to be unobservable by direct neutral sampling, yet in comparison, measurements in their ionized form provide a particularly sensitive method of detection. To better aid the interpretation of past measurements and planning of future observations, we present a model for the production of lunar pickup ions from the Moon consisting of two components: An analytic model for the distributions of 18 neutral species produced by various mechanisms and an analytic model for the ionization and subsequent acceleration of 20 exospheric and surface-sputtered pickup ion species. The dominant lunar pickup ions in the model are H_2^+, He^+, CO^+, $^{40}Ar^+$, Al^+, Na^+, K^+, Si^+, Ca^+, and O^+ with an asymmetric distribution favoring the positive interplanetary electric field hemisphere of the Moon. We compare the model predictions to statistically averaged pickup ion fluxes around the Moon as observed by the ARTEMIS spacecraft over the past decade. By filtering for interplanetary electric field-aligned, high-energy observations, we find that the pickup ion model lacks an additional source of heavy species. We suggest that a dense CO_2 exosphere of $3 \times 10^4 - 1 \times 10^5$ cm^{-3} could account for the missing pickup ion flux as part of the recycling of solar wind carbon ions incident to the Moon.

Plain Language Summary The Moon is surrounded by a thin neutral atmosphere comprised of multiple atomic and molecular species. This atmosphere, technically termed an "exosphere," is produced by multiple processes that are either internal or external to the Moon. As exospheric atoms and molecules are exposed to space, they are continuously ionized by photons, protons, and electrons from the Sun. Once ionized, these particles are accelerated by electromagnetic fields in interplanetary space and often lost from the Moon's environment. These "pickup ions" (so called because they are "picked up" into and carried along with the flow of particles in space by electromagnetic fields) provide information about the composition and distribution of the neutral lunar exosphere. We have constructed a model of 18 neutral and 20 ionized species in the lunar exosphere based on previous observations and/or models. The model predicts that the dominant pickup ion species in the lunar exosphere include carbon monoxide (CO^+), 40-argon ($^{40}Ar^+$), aluminum (Al^+), sodium (Na^+), and potassium (K^+). The model is compared to observations of lunar pickup ions by NASA's ARTEMIS mission. We find that the model is missing a component of the pickup ion flux and suggest that the Moon may harbor a dense carbon dioxide (CO_2) exosphere.

1. Introduction

While generally considered an airless body, the Moon in fact plays host to a tenuous and complex neutral exosphere generated via multiple distinct processes. Some exospheric generation processes are endogenous to the Moon, such as the effusion of ^{40}Ar from the lunar interior due to the decay of primordial ^{40}K (e.g., Benna et al., 2015; Hoffman et al., 1973; Hodges et al., 1974; Killen, 2002). Many other exospheric generation processes are due to exogenous inputs or forcing, including, for example, the neutralization and reemission of solar wind protons and alpha particles (He^{++}) as neutral H_2 (e.g., Hurley et al., 2017; Stern et al., 2013; Thampi et al., 2015) and He (e.g., Benna et al., 2015; Grava et al., 2021; Feldman et al., 2012; Hoffman et al., 1973; Hurley et al., 2015), respectively, sputtering of surface-bound species via charged particles originating from the solar wind or terrestrial magnetosphere (e.g., Vorburger et al., 2014; Wurz et al., 2007, 2022), or the vaporization of lunar regolith and/or incident micrometeoroid material by hypervelocity interplanetary micrometeoroid bombardment (e.g., Füri

et al., 2012; Hunten et al., 1998; Janches et al., 2021; Szalay et al., 2016). Many exospheric species at the Moon are in fact generated by multiple processes simultaneously introducing additional complexity in trying to untangle and distinguish the primary controls of the lunar exosphere as a whole.

A full accounting of lunar exospheric sources, sinks, and processes is critical for a broader understanding of lunar history and evolution. First and foremost, an understanding of the lunar exosphere is necessary for quantifying the fundamental physics of solid-surface interactions with the space environment (e.g., Wurz et al., 2022). Lessons learned at the Moon have significant extension and implications for space-surface interactions at other airless bodies throughout the solar system (e.g., Killen & Ip, 1999; Leblanc & Chaufray, 2011; Leblanc et al., 2022; Schörghofer et al., 2021). The lunar exosphere represents a potential avenue of transport for volatile species to migrate both into and out of cold-trapped regions near the lunar poles (e.g., Benna et al., 2019; Butler, 1997; Farrell et al., 2013; Hodges, 1991; Schörghofer et al., 2021). Such transport can occur both via relatively steady, long-term processes such as solar wind implantation or micrometeoritic influx (e.g., Crider & Vondrak, 2000; Füri et al., 2012) or via impulsive delivery and migration of volatiles from events such as cometary impacts (e.g., Ong et al., 2010; Prem et al., 2015; Stewart et al., 2011). Finally, knowledge of the outgassing and reimplantation rates of native lunar argon directly informs the lunar $^{40}Ar/^{36}Ar$ "antiquity" indicator, a widely used method of calibrating lunar sample ages (e.g., Eugster et al., 2001; Fagan et al., 2014). In particular, the scale height and spatial distribution of both argon isotopes control the rate at which ionized argon is implanted into the lunar regolith (e.g., Manka & Michel, 1970; Poppe, Halekas, Sarantos, & Delory, 2013), establishing a connection between exospheric space physics and geologic studies of the lunar surface.

A particularly sensitive method of studying the exosphere is via the detection of freshly ionized pickup ions, which are promptly accelerated from their birthplace by ambient electromagnetic fields such as from the solar wind or the terrestrial magnetotail (e.g., Hartle & Killen, 2006). Lunar pickup ions have been detected by several spacecraft both near to and remote from the Moon. The Active Magnetospheric Particle Tracers Explorer (AMPTE) spacecraft (Bryant et al., 1985) first reported the presence of lunar pickup ions downstream from the Moon in the solar wind, yielding constraints on the mass of the detected species to be between 23 and 37 amu (Hilchenbach et al., 1993). The Wind spacecraft, during a series of lunar flybys en route to L1, detected several instances of pickup ions originating from the Moon primarily at mass 16 (O^+ or CH_4^+), mass 27 (Al^+), and mass 28 (Si^+ or CO^+) (Mall et al., 1998). More recent measurements of lunar pickup ions have come from Kaguya (Tanaka et al., 2009; Yokota et al., 2009, 2014a, 2020), Chang'E−1 (Wang et al., 2011), the Acceleration, Reconnection, Turbulence, and Electrodynamics of the Moon's Interaction with the Sun (ARTEMIS) mission (Halekas et al., 2012, 2013, 2016, 2018; Harada et al., 2015; Liuzzo et al., 2021; Poppe et al., 2012, Poppe, Halekas, Samad, et al., 2013; Zhou et al., 2013), and the Lunar Atmospheric and Dust Environment Explorer (LADEE) mission (Halekas et al., 2016; Poppe et al., 2016). Together, these observations have confirmed the presence of multiple additional exospheric species including H_2^+, He^+, C^+, O^+, Ne^+, Na^+, Al^+, Si^+/CO^+, K^+, and $^{40}Ar^+$. Spatial distributions of neutral species can also be inferred at times, including, for example, dawn-dusk asymmetries in the Na and K neutral distributions that indicate complex nightside recycling of exospheric species (Yokota, Tanaka, et al., 2014) and the presence of relatively large neutral scale heights that indicate contributions from energetic release processes such as charged-particle sputtering and/or micrometeoroid impact vaporization (Halekas et al., 2018).

Lunar pickup ions can also contribute to and impact the lunar and terrestrial plasma environments. Observations have shown that lunar exospheric pickup ions may alter the Moon's electrodynamic environment in low-density ambient plasmas by providing a source of mass and current (e.g., Cao, Halekas, Poppe, et al., 2020; Liuzzo et al., 2021; Zhou et al., 2014). In particular, while in the low-density magnetotail lobes, lunar pickup ions contribute to a lunar ionosphere that exceeds the ambient lobe plasma density by a factor of several in regions immediately sunward of the Moon (Halekas et al., 2018; Poppe et al., 2012). Pickup ion observations can also be used as tracer species for determining terrestrial magnetotail convection speeds, enabling correlative studies between magnetospheric convection rates in the tail and upstream solar wind and interplanetary magnetic field conditions (Cao, Halekas, Chu, et al., 2020). Finally, the outflow and recirculation of lunar pickup ions that escape the immediate lunar vicinity can also be detected in long-term averages of Geotail ion composition observations both within and outside of the terrestrial magnetosphere, indicating that lunar pickup ions contribute to the plasma composition of Earth's magnetosphere (Christon et al., 2020).

Given the wealth of recent lunar exospheric and pickup ion measurements in the last decade, it is worthwhile to compile a comprehensive census of the production rates and spatial distributions of lunar pickup ions. A decade's worth of lunar pickup ion observations by the ARTEMIS spacecraft in orbit around the Moon provide a statistically rich data set with which to compare to such a model, notwithstanding ARTEMIS' lack of ion compositional measurements. Upcoming mass-resolved ion measurements by NASA's Heliophysics Environmental and Radiation Measurement Experiment Suite (HERMES) to be hosted on the Lunar Gateway offer an opportunity for further insight into the compositional and spatial makeup and variability of lunar pickup ions and by extension, the lunar exosphere. The goal of this study is to incorporate recent measurements of both the neutral and ionized components of the lunar exosphere into a single predictive model that can be used for analysis of past data sets and planning for future data sets of lunar pickup ion observations. In Section 2, we describe both the neutral and ionized portions of the lunar exospheric pickup ion model. Section 3 presents results from the model, including neutral density distributions, total ion production rates, and pickup ion flux distributions. Section 4 compares the model predictions to a statistical aggregation of in situ ARTEMIS observations of lunar pickup ion fluxes based on the methodology outlined in Harada et al. (2015). Finally, we discuss the implications of our results, especially with regard to future in situ measurements of pickup ion fluxes at the Moon, and conclude in Section 5.

2. Model Description

To model and predict the distribution of pickup ions in near-lunar space, we have constructed an analytical model consisting of two major parts. The first part of the model describes the neutral density distributions for 18 distinct species generated by up to six separate processes, see Table 1. Species can be generated by a single process or by multiple overlapping, noninteracting processes. The specific spatial distributions and overall magnitude of the densities are taken from in situ or remote-sensing observations, where available. In cases where observations have not been reported, theoretical predictions and/or upper limits are chosen. The second part of the model describes the ionization and charged-particle dynamics of pickup ions generated from the modeled neutral distributions. Exospheric neutral particles are ionized via three processes: Photoionization (including photodissociative ionization of molecular species), charge exchange with solar wind protons, and electron impact ionization. Additionally, we also include at this step ionized products originating directly from charged-particle sputtering of the lunar surface (Elphic et al., 1991). Pickup ion fluxes are then calculated based on the spatial distribution of ion production rates and an analytic description for pickup ion trajectories in specified solar wind and interplanetary magnetic field (IMF) conditions (e.g., Hartle & Killen, 2006).

We emphasize that the nature of this model is to use time-independent analytic descriptions for both the neutral density distributions and pickup ion dynamics, instead of more complex and computationally intensive neutral Monte Carlo (e.g., Grava et al., 2015; Hurley et al., 2016; Killen et al., 2012; Lee et al., 2011; Sarantos & Tsavachidis, 2021) or ion particle-tracing techniques (e.g., Cladis et al., 1994; Poppe, Halekas, Samad, et al., 2013). Thus, the model does not, for example, track individual macroparticles (for either neutral or ionized species) through a grid-based domain or use time-dependent inputs from, for example, upstream solar wind variability or ionization rate variability. The models are intended to represent the mean, steady-state conditions for both neutral particles and pickup ions in the lunar environment (see Section 5 for more detailed discussion on time variability). Additionally, the model deliberately simplifies some aspects of both the neutral exosphere and the pickup ion distributions. The greatest simplification likely originates in the neutral distributions, as our analytic descriptions do not necessarily take into account complex processes such as the effects of solar radiation pressure of Na and K dynamics (e.g., Ip, 1991; Matta et al., 2009; Smyth & Marconi, 1995; Wilson et al., 2003) or reactions between individual atoms and the lunar surface that may alter equilibrium density distributions (e.g., Sarantos & Tsavachidis, 2020, 2021). Nevertheless, the model is constructed in such a way that future three-dimensional neutral distributions for any species derived from such Monte Carlo methods can easily replace any of the analytic distributions in the model, if so desired.

2.1. Neutral Distribution Modeling

In the neutral exospheric portion of the model, we have identified six general types of neutral distributions based on either their formation mechanism or fundamental physical behavior at the Moon. These types include (a) thermally desorbed, (b) sputtered via charged-particle impact, (c) photon-stimulated desorbed, (d) micrometeoroid impact vaporized (MIV), (e) argon, and (f) carbon-bearing species. Along with the detailed descriptions

Table 1
The Constituent Species of the Neutral and Ionized Exospheric Model Including the Species Name, Neutral Mass, M_n, Ionized Mass, M_i, Photoionization Rate, R_{ph}, Charge Exchange Rate, R_{cx}, Electron Impact Ionization Rate, R_{ei}, and the Reference Neutral Densities for Thermal (Thm), Sputtered (Spt), MIV, Photon-Stimulated Desorption (PSD), Argon, and Carbon-Bearing Neutral Species, Respectively

Species	M_n	M_i	R_{ph}	R_{cx}	R_{ei}	Thm	Spt	MIV	PSD	Argon	Carbon
H_2	2.0	2.0	8.45e−8	6.97e−10	5.85e−9	2.50e+3	-	-	-	-	-
He	4.0	4.0	1.12e−7	4.48e−9	5.00e−11	2.50e+3	-	-	-	-	-
C	12.0	12.0	6.00e−6	-	9.08e−8	-	1.05e+0	2.00e+0	-	-	-
O	16.0	16.0	1.33e−6	1.89e−7	3.48e−8	-	8.8e+0	6.63e+1	-	-	-
CH_2 (CH_4)	16.0	14.0	3.83e−8	-	4.66e−9	-	-	-	-	-	4.60e+2
CH_3 (CH_4)	16.0	15.0	3.27e−7	-	1.13e−8	-	-	-	-	-	4.60e+2
CH_4	16.0	16.0	6.00e−7	6.30e−7	1.46e−8	-	-	-	-	-	4.60e+2
Ne	20.0	20.0	3.86e−7	5.84e−10	1.50e−8	2.50e+3	-	-	-	-	-
Na	23.0	23.0	7.59e−6	8.40e−7	5.00e−7	3.50e+1	5.25e−2	3.00e−1	2.00e+0	-	-
Mg	24.3	24.3	9.08e−7	2.10e−7	1.00e−6	-	1.20e+0	5.50e+0	-	-	-
Al	27.0	27.0	1.25e−3	2.10e−7	7.50e−7	-	2.50e−1	8.40e−1	-	-	-
Si	28.0	28.0	3.55e−5	2.10e−7	5.00e−7	-	8.10e−1	3.10e0	-	-	-
CO	28.0	28.0	6.70e−7	4.20e−9	5.23e−8	-	-	-	-	-	1.40e+4
O (CO)	28.0	16.0	5.36e−8	-	3.89e−9	-	-	-	-	-	1.40e+4
C (CO)	28.0	12.0	6.41e−8	-	1.74e−9	-	-	-	-	-	1.40e+4
^{36}Ar	36.0	36.0	5.58e−7	2.37e−7	1.00e−7	-	-	-	-	1.60e+3	-
K	39.0	39.0	2.74e−5	1.28e−6	7.50e−7	8.00e+0	1.50e−2	5.00e−2	5.00e−1	-	-
Ca	40.0	40.0	3.15e−4	2.10e−7	5.50e−7	-	5.25e−2	1.00e−1	-	-	-
^{40}Ar	40.0	40.0	5.58e−7	2.37e−7	1.00e−7	-	-	-	-	5.00e+4	-
CO_2	44.0	44.0	1.21e−6	6.30e−9	5.98e−8	-	-	-	-	-	1.25e+2
CO (CO_2)	44.0	28.0	1.08e−7	-	6.35e−9	-	-	-	-		1.25e+2
O (CO_2)	44.0	16.0	1.38e−7	-	5.41e−9	-	-	-	-	-	1.25e+2
C (CO_2)	44.0	12.0	6.80e−8	-	1.81e−9	-	-	-	-	-	1.25e+2
Ti	47.0	47.0	4.07e−6	2.10e−7	5.00e−7	-	2.60e−1	5.00e−1	-	-	-
Fe	56.0	56.0	1.38e−5	2.10e−7	4.00e−7	-	2.3e+0	4.10e+0	-	-	-

Note. Masses are in units of amu, ionization rates are in units of s^{-1}, and densities are in units of cm^{-3}. Species with parent molecules in parentheses are those produced by dissociative ionization. Note that we use the average chemical mass for Mg (24.3 amu) as opposed to individual isotopes.

below, the reference neutral densities compiled for each species and each process are detailed in Table 1. Note that densities for the thermal, sputtered, and PSD-produced species are quoted with respect to the lunar subsolar point, densities for MIV-produced species and argon isotopes are quoted with respect to the dawn terminator, and carbon-bearing species are quoted with respect to their peak.

The "thermal" distribution denotes those species that accommodate (either partially or fully) to the local lunar surface temperature, do not adsorb on the lunar nightside, and can generally be described by the noncondensable gas law (Benna et al., 2015; Hodges & Johnson, 1968). Molecular hydrogen (H_2), helium (He), and neon (Ne) are modeled as thermal species. All three of these species are believed to be primarily sourced from the solar wind, with some contribution from endogenous radioactive decay in the case of helium (Benna et al., 2015; Das et al., 2016). Additionally, we include thermal distributions for Na and K based on the detection of thermally equilibrated (or "cold") components in remote-sensing observations (e.g., Potter & Morgan, 1988, 1998). For the lunar surface temperature at a given location, we use the analytic expression from Hurley et al. (2015) based on LRO/Diviner observations and make the simplifying assumption that the radial column of exospheric neutral density is fully accommodated to the lunar surface temperature immediately underfoot. Figure 1a shows the neutral distribution of thermal He in the lunar equatorial plane as an example.

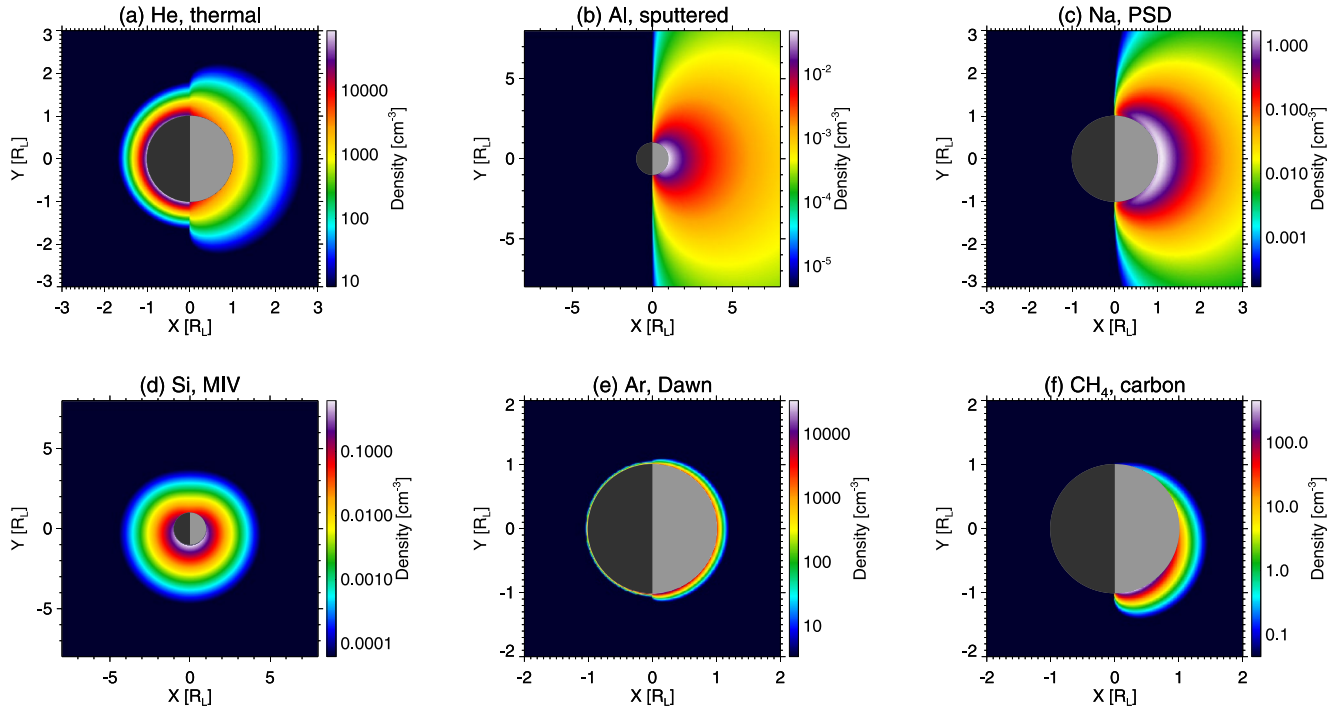

Figure 1. Exospheric neutral density distributions for select species in the lunar equatorial plane for each exospheric distribution type: (a) Helium as a thermal species, (b) aluminum as a solar wind sputtered species, (c) sodium as a photon-stimulated desorption species, (d) silicon as a micrometeoroid impact vaporization species, (e) argon species, and (f) methane as a carbon-bearing species. Sunlight and the solar wind are incident from the right.

Charged-particle sputtering is known to be a major source of refractory elements in the lunar exosphere. The underlying physical mechanisms of sputtering have long been studied both theoretically and experimentally (e.g., Baragiola et al., 2002; Baragiola, 2004; Barghouty et al., 2011; Behrisch & Eckstein, 2007; Biersack & Eckstein, 1984; Cassidy & Johnson, 2005; Dukes et al., 2011; Elphic et al., 1991; Hijazi et al., 2014; Johnson & Baragiola, 1991; Johnson & Leblanc, 2001; Meyer et al., 2011; Wurz et al., 2007; Szabo et al., 2018, 2020). At the Moon, the solar wind is the dominant source of charged particles with energies sufficient to induce sputtering, with additional contributions from passage through the terrestrial magnetosheath and magnetotail (for a discussion of the mean charged particle flux to the Moon as a function of lunar phase, see Poppe et al. (2018)). Laboratory observations have demonstrated that sputtered atoms are typically emitted with a Sigmund-Thompson (S-T) distribution (Husinsky et al., 1985; Sigmund, 1969; Thompson et al., 1968), which we adopt for all sputtered species. Compared to a Maxwellian distribution, the S-T distribution has an extended tail to higher energies leading to a more extended neutral distribution (see also Wurz et al., 2007). Furthermore, sputtered species are only considered to be emitted from the dayside of the Moon despite the potential presence of off-axis particle fluxes in the terrestrial foreshock (e.g., Nénon & Poppe, 2021; Nishino et al., 2017) We also do not consider second-order effects in the sputtered distribution at the Moon from either self-sputtering (Poppe, Halekas, Sarantos, & Delory, 2013) or local shielding by crustal magnetic anomalies (e.g., Vorburger et al., 2012; Poppe et al., 2014; Halekas et al., 2016). Sputtered species include carbon (C), oxygen (O), sodium (Na), magnesium (Mg), aluminum (Al), silicon (Si), potassium (K), calcium (Ca), titanium (Ti), and iron (Fe). Figure 1b shows the neutral distribution of sputtered Al as an example.

Photon-stimulated desorption (PSD) is a process whereby the absorption of a solar photon yields a subsequent desorption of a neutral atom from the lunar regolith (Yakshinskiy & Madey, 1999, 2004). At the Moon (as well as Mercury and potentially other airless bodies), PSD is effective for sodium (Na) and potassium (K) (e.g., Mendillo & Baumgardner, 1995; Potter & Morgan, 1988, 1991, 1998; Potter et al., 2000). We model the PSD species on the lunar dayside with a cosine solar zenith angle distribution and a Weibull velocity distribution as described by Gamborino and Wurz (2018) to fully capture the non-Maxwellian nature of the PSD velocity distribution (Yakshinskiy & Madey, 2004). For simplicity, we adopt the same velocity distribution for PSD emission of K as well. As noted above, we do not model the effects of solar radiation pressure on the equilibrium Na and K

distributions e.g., Ip, 1991; Smyth & Marconi, 1995; Wilson et al., 2003; Matta et al., 2009). As such, the Na and K neutral distributions will not possess the observed "tail"-like structures due to antisunward-accelerated neutral species. Figure 1c shows the neutral distribution of Na released via PSD.

Micrometeoroid impact vaporization is the production of neutral species from the lunar regolith upon the hypervelocity impact of an incident micrometeoroid (e.g., Collette et al., 2014; Eichhorn, 1976, 1978). The spatial distribution of MIV-produced neutral species is taken from constraints on the primary impacting interplanetary micrometeoroid flux based on in situ observations of secondary meteoroid ejecta by the LADEE/Lunar Dust Experiment (LDEX) instrument (Horányi et al., 2015; Janches et al., 2018; Pokorný et al., 2019; Szalay & Horányi, 2015). Impacting micrometeoroids peak near dawn with a broad extent past noon and midnight and a minimum near dusk (e.g., Figure 1 of Szalay & Horányi, 2015). We empirically characterize the local time distribution of MIV-produced neutral species, $f(\phi)$, as follows:

$$f(\phi) \propto 0.9\ \ (0.5 + 0.5\cos\phi) + 0.1, \tag{1}$$

where ϕ is the angle with respect to dawn (6 LT). Laboratory experiments have demonstrated that MIV-produced neutral species have characteristic temperatures of T = 2,500–5000 K with a positive, linear correlation of temperature with micrometeoroid impact velocity (Collette et al., 2013, 2014; Eichhorn, 1978). Here, we adopt an intermediate value of T_{miv} = 3750 K, neglecting any local changes in exospheric neutral temperature that may arise from varying impactor speeds (e.g., Pokorný et al., 2019). Neutral species generated by micrometeoroid impact vaporization are identical to those produced via charged-particle sputtering, specifically, C, O, Na, Mg, Al, Si, K, Ca, Ti, and Fe. Note that we elect not to include the potential effect of metal-oxide formation in the micrometeoroid-impact plume due to the lack of a preexisting model for this process at the Moon. We do note that oxide formation from micrometeoroid bombardment has previously been suggested as a relevant process at Mercury (e.g., Berezhnoy & Klumov, 2008; Berezhnoy, 2018; Killen et al., 2005; Killen, 2016; Valiev et al., 2020), thus future modeling and characterization of this effect at the Moon is identified as a potential avenue of research.

The fifth type of neutral distribution used here pertains specifically to argon, including both the ^{36}Ar and ^{40}Ar isotopes. Argon has been known to exist in the lunar exosphere since Apollo observations on the lunar surface (Hodges et al., 1973, 1974; Hodges, 1975, 1980; Hoffman et al., 1973), sourced from both the solar wind as the ^{36}Ar isotope and from decay of endogenous lunar ^{40}K into ^{40}Ar (e.g., Hodges & Hoffman, 1975; Killen, 2002). Note that the ^{38}Ar isotope has also been observed in the solar wind (Weygand et al., 2001); however, its abundance is more than five times less than that of ^{36}Ar in the solar wind and thus, we neglect its presence in the current model (although it should behave similarly to ^{36}Ar in the lunar exosphere). More recent measurements by the LADEE NMS instrument of ^{40}Ar have confirmed the Apollo detections of endogenous argon and documented several periodic variabilities, including evidence for localized sources (Benna et al., 2015; Hodges & Mahaffy, 2016; Kegerreis et al., 2017). To model the neutral distributions of both ^{36}Ar and ^{40}Ar, we use the recent modeling work of Grava et al. (2015) combined with in situ measurements from the LADEE/NMS instrument for ^{40}Ar (Benna et al., 2015) and measurements by the Apollo 17 Lunar Mass Spectrometer for ^{36}Ar (Hoffman & Hodges, 1975). Figure 1e shows the neutral distribution for ^{40}Ar.

The final type of neutral distribution is applied to carbon-bearing species, including methane (CH_4), carbon monoxide (CO), and carbon dioxide (CO_2). Early indications of carbonaceous species in the lunar exosphere were reported by Hoffman and Hodges (1975) based on observations by the Apollo 17 Lunar Mass Spectrometer (LMS) on the lunar surface. Specifically, CH_4 and CO_2 were detected at statistically significant levels just prior to dawn, although Hodges (2016) later suggested that these detections may have been outgassed contaminants from Apollo equipment left on the lunar surface. Later observations by the LADEE Neutral Mass Spectrometer (NMS) provided a clear detection of CH_4 in the lunar exosphere (Hodges, 2016), characterized by a strong near-dawn density enhancement typical of condensable species that freeze out to the lunar nightside surface and are remitted near- or postdawn as the lunar surface warms (i.e., similar to ^{36}Ar and ^{40}Ar). Halekas et al. (2015) further reported statistically significant detections of mass 12 (C^+) and mass 28 ions with LADEE/NMS ion mode observations. While an absolute identification of mass 28 is not strictly possible due to the overlap of N_2^+, CO^+, and Si^+, Halekas et al. (2015) argued that CO^+ was the most probable candidate due to the relatively low ionization rate of N_2, the stringent limits on Si neutral densities from Cook et al. (2013), and the contemporaneous mass 12 (C^+) signal, which could possibly be due to photodissociative ionization of CO (or also CO_2). For CH_4, we base the

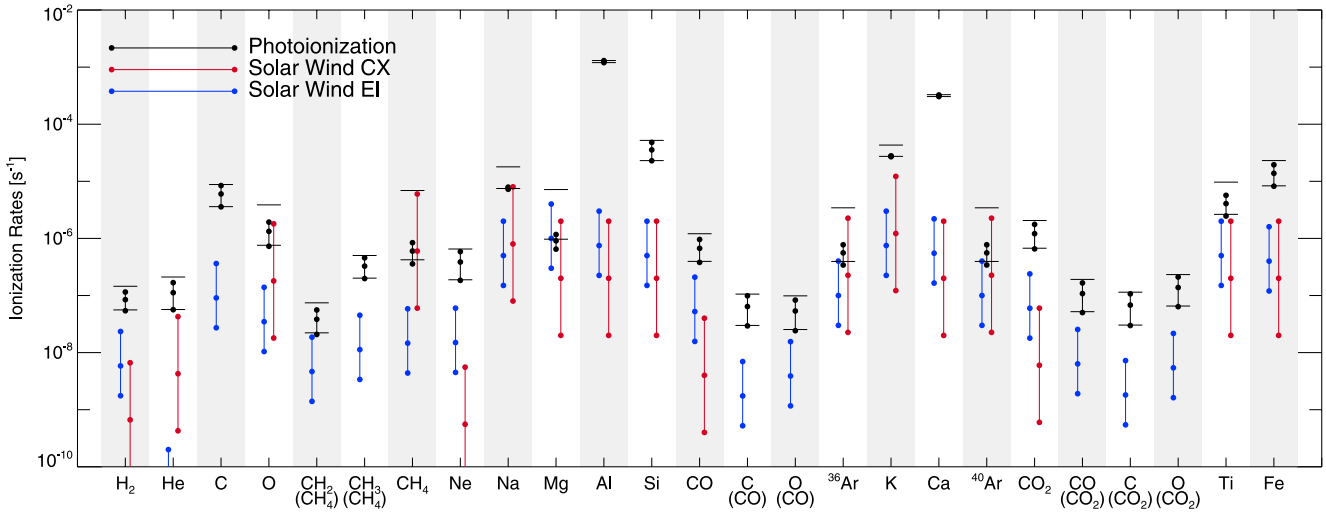

Figure 2. The photo, solar wind charge exchange, and electron impact ionization rates by species. Photoionization (black) is shown for solar minimum, median, and maximum conditions. Solar wind charge exchange and solar wind electron impact ionization rates are shown for the 2-σ range in solar wind proton flux and solar wind electron density, respectively (Dmitriev et al., 2011). Ion species generated via dissociative ionization (e.g., $CO + e^- \rightarrow C^+ + O + 2e^-$ or $CO + e^- \rightarrow C + O^+ + 2e^-$) are denoted with parent molecules in parentheses. The pair of horizontal lines for each species denotes the minimum and maximum total ionization rates (i.e., the sum over photo, electron impact, and charge exchange ionization).

modeled neutral density distribution on Hodges (2016), which possesses peak densities near 7–8 local time. For CO, we take the estimated density from Halekas et al. (2015) based on the assumption that the mass 28 signal observed in LADEE/NMS ion mode observations is due solely to CO^+ and not N_2^+ or Si^+. For CO_2, we estimate an upper limit density based on the nondetection of CO_2^+ ions by the LADEE/NMS ion mode observations. The spatial distributions for all three carbon-bearing species are adopted from Hodges (1976) and Hodges (2016). Specifically, the CH_4 distribution has a peak in the neutral density slightly postdawn (7–8 LT) followed by a rapid exponential decay across the lunar dayside, while the CO and CO_2 spatial distributions are much more broadly extended across the lunar dayside.

It is worth noting here the lack of OH and/or H_2O distributions in our model. Both species have been detected adsorbed to the lunar surface (e.g., Clark, 2009; Honniball et al., 2021; Li & Milliken, 2017; Pieters et al., 2009; Sunshine et al., 2009) and the LADEE/NMS investigation reported the detection of water related to meteoritic impacts liberating a buried layer of increased hydration (Benna et al., 2019; Hurley & Benna, 2018). In contrast, remote spectroscopic searches have yielded only upper limits for OH and/or H_2O (e.g., Stern et al., 1997; Wang et al., 2015) and in situ ion mode observations by LADEE/NMS were deemed as likely outgassing of spacecraft contaminants (Halekas et al., 2015). Previous Monte Carlo-type neutral models have explored the production, transport, and sequestration of OH/H_2O at the Moon (e.g., Crider & Vondrak, 2000; Schorghofer, 2014, 2015; Schorghofer et al., 2017); yet many of these predictions remain untested, and a unified and observationally validated model of the OH or H_2O exospheres at the Moon is not yet in hand. Thus, we do not currently include these species in our modeling; however, future investigations with the model can be used to place constraints on the abundance of OH or H_2O in the lunar exosphere via comparison with existing in situ charged-particle measurements (e.g., see Section 4) or to make predictions for future in situ instrumentation focused on exospheric water.

2.2. Pickup Ion Modeling

The second portion of the model calculates the production rates of lunar exospheric ions and follows their dynamics as they are picked up into the solar wind flow. For each neutral species, we calculate the total ionization rate by including photoionization by solar irradiation, charge exchange with solar wind protons, and electron impact ionization by solar wind electrons. We surveyed a broad range of literature to compile all three ionization rates for all species, where available, and display these rates in Figure 2. For photoionization rates, we primarily relied on Huebner and Mukherjee (2015) and retrieved photoionization rates for solar minimum, median, and maximum conditions. Additionally, we included photodissociative ionization for the neutral molecular species, CH_4, CO,

and CO_2 using appropriate branching ratios. Thus, CH_4 neutral molecules give rise to CH_4^+, CH_3^+, and CH_2^+ (we neglected both CH^+ and H^+ formation due to their very low branching ratios), CO gives rise to CO^+, O^+, and C^+, and CO_2 gives rise to CO_2^+, CO^+, O^+, and C^+. For solar wind proton charge exchange and solar wind electron impact ionization, we used median solar wind conditions but show the expected variability for both processes in Figure 2.

Across all species in the model, ionization rates vary over at least eight orders of magnitude. For most species, photoionization is the dominant ionization mechanism, particularly in the cases of H_2^+, C^+, Al^+, Si^+, K^+, Ca^+, and Fe^+. In some cases, the solar wind charge exchange or electron impact ionization rates equal or exceed photoionization rates, such as for O^+, CH_4^+, Na^+, Mg^+, and $^{36}Ar^+/^{40}Ar^+$. Thus, it is critical to include all three processes when calculating the net pickup ion fluxes at the Moon (and by extension at other airless bodies exposed to the solar wind throughout the solar system). Variability in the range between minimum and maximum ionization rates can also be seen across different species. For example, the total ionization rate of Al^+ is dominated by photoionization, which varies extremely little over solar cycle and thus dwarfs any variability contributed from solar wind charge exchange or electron impact ionization. In comparison, the total ionization rates for CH_4 and Ar vary by over an order of magnitude even when summed across all three ionization processes. This variability, notwithstanding, we use the sum of the median ionization rates for all three processes as the total ionization rate per species throughout the rest of this study. A study of pickup ion variability over various ionization conditions is left for future work.

At this point in the model, we also include the production of lunar pickup ions generated directly from the surface via impact of solar wind protons (Elphic et al., 1991; Dukes & Baragiola, 2015). We generate surface-sputtered ions for Na^+, Mg^+, Al^+, Si^+, K^+, Ca^+, Ti^+, and Fe^+ with a cosine solar zenith angle dependence. The magnitudes of the fluxes for these surface-sputtered ions at the subsolar point are taken from Elphic et al. (1991) (see their Figure 4). We note that McLain et al. (2011) has also reported the production of surface ions via electron-stimulated desorption (ESD), which should also contribute to the surface ion flux at the Moon. The production of surface ions via ESD, however, is dominated (~90%) by the production of H^+ ions (i.e., Figure 2 of McLain et al. (2011)), with only minor contributions from species such as O^+, Na^+, and K^+. Taking this into account, the contribution of ESD-produced surface ions is likely negligible compared to the production of surface ions via proton bombardment and thus, we do not explicitly include an ESD-generated term. We do note, however, that the spatial distribution of any ESD-generated ions would be nearly identical to that of solar wind proton-sputtered ions and thus relatively indistinguishable.

Finally, to trace the pickup ion trajectories and calculate pickup ion fluxes in near-lunar space, we employ a simple analytical model for the motion of freshly born pickup ions (Hartle & Killen, 2006), which specifies the trajectory $[x, y]$ of an individual pickup ion as follows:

$$x = x_o - r_g(\theta\pi + \sin\theta) \tag{2}$$

$$y = y_o + r_g(1 + \cos\theta) \tag{3}$$

where $[x_o, y_o]$ is the starting position of the ion, $r_g = m_i v_{sw}/qB$ is the ion gyroradius, θ is an angular coordinate, m_i is the ion mass, v_{sw} is the solar wind velocity, $q \equiv +1e$ is the charge of the ion, and B is the magnitude of the interplanetary magnetic field. Lunar gravity is neglected in comparison to the electromagnetic forces. The solar wind velocity and IMF strength are assumed to be constant in both space and time and for simplicity, we set them fully perpendicular to one another. We assume that the pickup ion generation is insufficient to measurably perturb that incident solar wind at the Moon, such that we can safely employ a test-particle approach. Previous analyses of ARTEMIS observations in the magnetotail have shown only very minor perturbations to the magnetotail environment (e.g.,Liuzzo et al., 2021; Poppe et al., 2012; Zhou et al., 2014) and given the higher number and momentum density present in the solar wind, this assumption is well grounded. We also note that we do not at present model lunar pickup ion dynamics in the terrestrial magnetosheath or terrestrial magnetotail. Such investigations are left for future work. We neglect any initial velocity that the parent neutral may possess, as such velocities are quickly dwarfed by acceleration of the ions in interplanetary space. We also neglect the influence of any perturbations of the electromagnetic field environment around the Moon that arise from the lunar wake (e.g., Halekas, Brain, & Holmström, 2014; Holmström et al., 2012; Xu et al., 2019; Zhang et al., 2014) or lunar crustal magnetic anomalies (e.g., Halekas, Poppe, et al., 2014, 2017; Lue et al., 2011). The ion trajectories are analytically computed until

the trajectory either impacts the Moon or the trajectory leaves the model domain, which extends downstream to 12 lunar radii and at least 8 lunar radii laterally.

3. Model Results

3.1. Spatial Distributions of Neutral Species

Figure 3 shows the spatial density distributions for all 18 neutral species in the equatorial plane of the Solar-Selenocentric-Ecliptic (SSE) frame, each summed over all relevant production processes. The SSE frame is oriented such that the $+x$ axis points from the Moon to the Sun, the $+z$ axis points to ecliptic north, and the $+y$ direction completes the right-handed set. The spatial distribution of each neutral species reflects the dominant production mechanism(s) at play as well as the mass of the neutral species (which governs the scale height). The thermally equilibrated but noncondensing species (H_2, He, and Ne) display strong dayside/nightside asymmetries in line with the steep change in surface temperature as a function of local time (i.e., Hodges & Johnson, 1968; Hurley et al., 2015). We note that the sharp change in scale heights seen in these three species at the terminators is due to the analytical simplification of assigning the local scale height to immediately reflect the local surface temperature. In reality, the change in exospheric scale height seen in these species will likely be more gradual due to lateral mixing of particles as they migrate from warmer to colder regions (e.g., Hodges & Johnson, 1968; Tucker et al., 2019). Refractory elements that are released into the exosphere via the relatively energetic processes of charged-particle sputtering and micrometeoroid impact vaporization have the most extended neutral distributions. Particular examples of such 'hot' species include C, O, Mg, Al, Si, Ca, Ti, and Fe. In these cases, the sum of the neutral spatial distributions from charged-particle sputtering, which is hotter but only occurs on the dayside, and MIV, which is relatively cooler but extends through the nightside, yields dayside/nightside asymmetries in the total density distributions of these species. In comparison, the density distributions of Na and K are dominated at low altitudes by their thermal components with broad dayside extensions due to PSD. Additionally, contributions from charged-particle sputtering and MIV are present for both species, particularly at high altitudes ($>\sim 2$ R_L) and on the lunar nightside. Again, we note here that the Na and K distributions presented here do not account for the effect of solar radiation pressure, which will deform and extend these distributions hundreds of Earth radii tailward (e.g., Lee et al., 2011; Line et al., 2012; Mierkiewicz et al., 2006). Finally, both the argon isotopes and CH_4 display clear dawn-dusk asymmetries due to the nightside adsorption and delayed postdawn reemission (e.g., as seen in Hodges (2016) for CH_4), while CO and CO_2 are symmetrically distributed about the lunar subsolar point. Scale heights are generally small for these species (ranging between ~45 km for CO_2 and ^{40}Ar to ~125 km for CH_4) given the assumed surface-temperature equilibrium and/or relatively high masses for these species.

3.2. Spatial Distributions of Pickup Ions

Figure 4a presents the total ion production rate for the lunar exosphere summed over all neutral species and all ionization processes (including all photodissociative ionization branches, where applicable) in the lunar equatorial SSE plane. Ion production from the lunar exosphere is strongest immediately above the dayside lunar surface yet also extends broadly to altitudes of several lunar radii on the lunar dayside driven by hotter and therefore more spatially extended species produced by charged-particle sputtering and/or MIV. Additionally, ion production occurs downstream from the lunar terminator along the flanks of the lunar optical shadow due to the broad local time extent of MIV-produced neutral species, as well as contributions from thermally desorbed species that do not condense out to the lunar nightside (i.e., H_2, He, Ne). Total ion production rates show a relatively large dawn-dusk asymmetry, with near-surface ion production rates at dawn nearly 30 times larger than near-surface ion production rates at dusk. At low altitudes, this is primarily driven by the underlying dawn-dusk asymmetry of the ^{36}Ar and ^{40}Ar neutral distributions, while at higher altitudes the dawn-dusk asymmetry of MIV-produced neutral species also contributes.

The relative distribution of species contributing to the total ion production rate is complex, as illustrated in the vertical ion production profiles at the dawn terminator and subsolar points, shown in panels 4(b) and (c), respectively. The presence of neutral distributions with distinct characteristic temperatures and scale heights (i.e., thermal desorption in the hundreds of K; PSD, MIV, and charged-particle sputtering in the thousands of K) yields a total vertical ion production rate profile with multiple distinct power-law profiles, breaking near 100 km at dawn and near 500 km at the subsolar point. At dawn, the maximum total ion production rate is

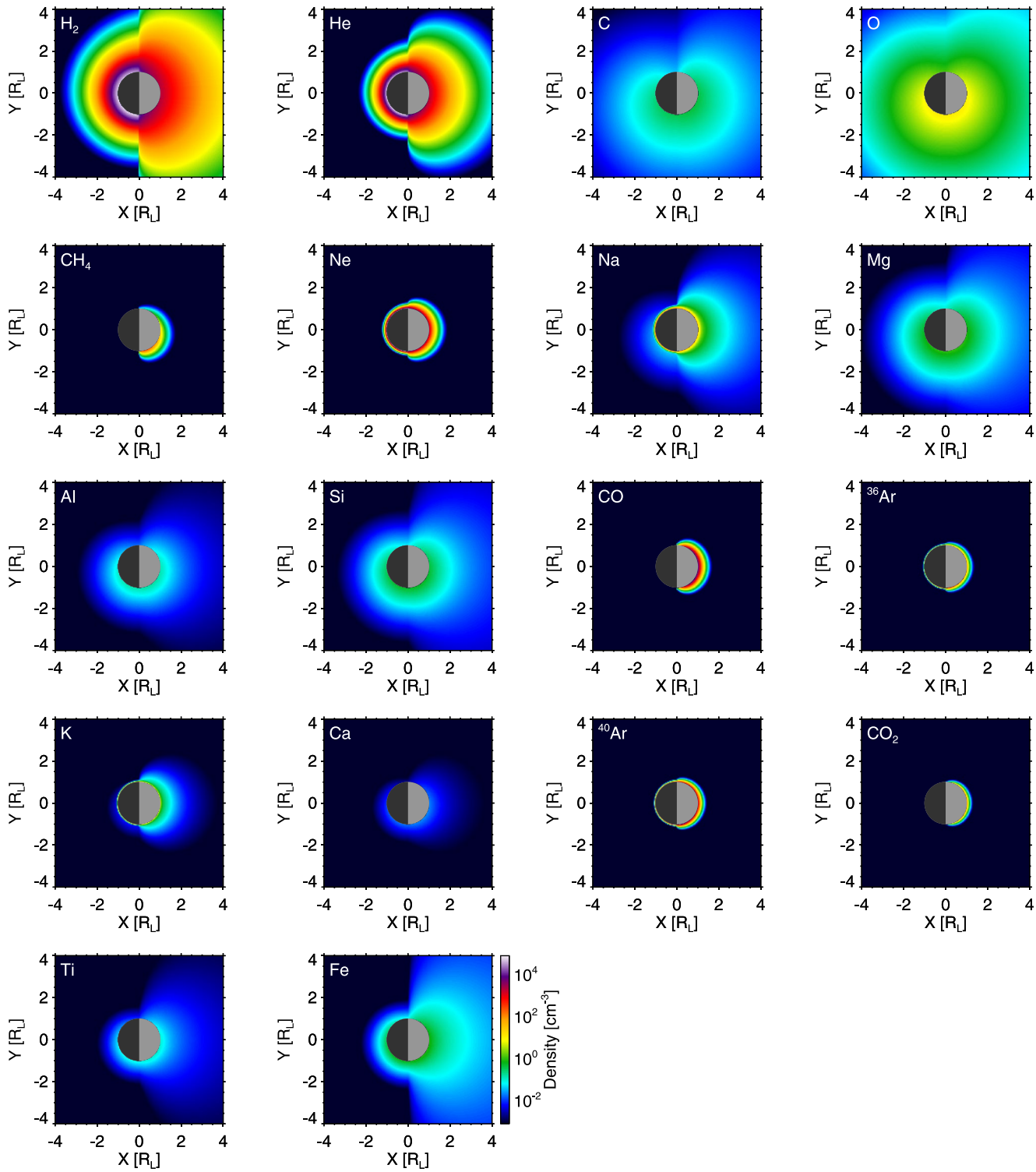

Figure 3. Exospheric neutral density distributions for all species in the lunar exosphere combined over all possible sources for each species.

$\sim 6 \times 10^{-2}$ cm^{-3} s^{-1}, dominated by the local production of thermally desorbed $^{40}Ar^{+}$. Other species, such as Ne^{+}, He^{+}, Na^{+}, H_2^{+}, K^{+}, and $^{36}Ar^{+}$ contribute to the total ion production rate at dawn at altitudes less than 100 km at levels between ~2 and 15% compared to $^{40}Ar^{+}$ production, with all other species contributing <1% relative to $^{40}Ar^{+}$. At altitudes above ~150 km, species with larger scale heights dominate the local ion production rate,

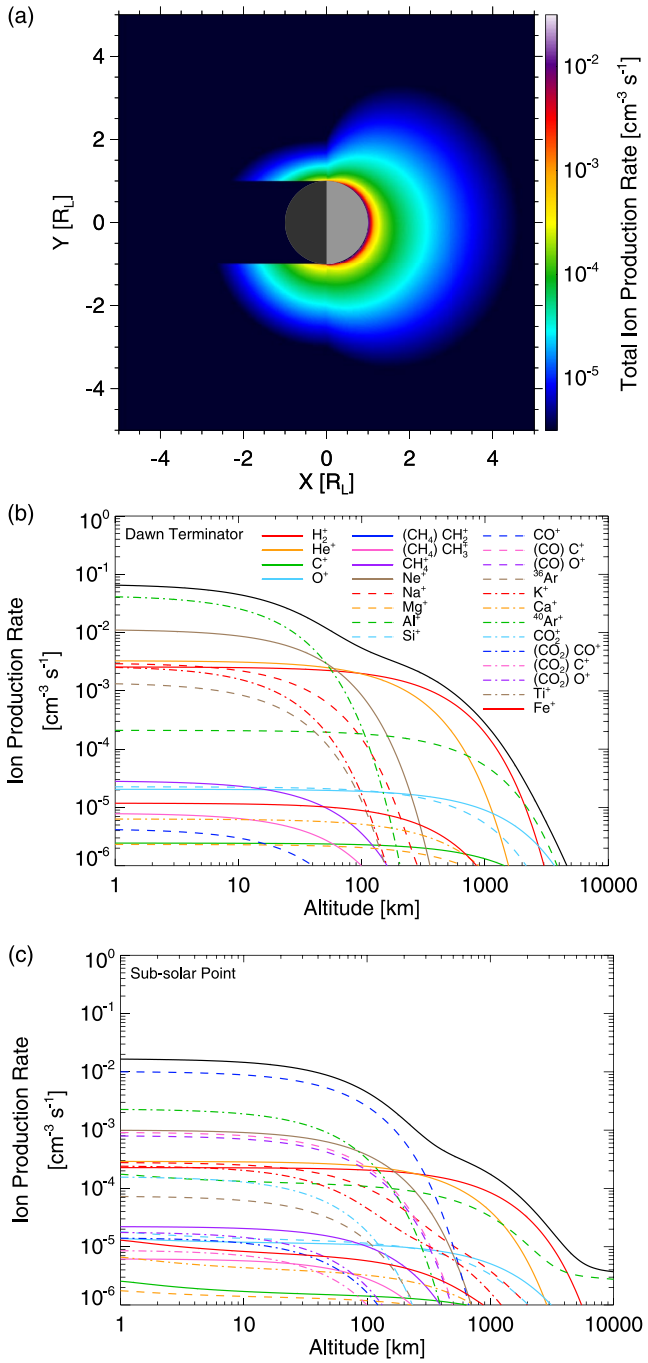

Figure 4. (a) The spatial distribution of the total ion production rate summed over all neutral species and all three ionization mechanisms in the lunar equatorial plane. Additionally, the vertical profiles of the ion production rate by species above the (b) lunar dawn terminator and (c) subsolar points, respectively. In both panels, the total ion production rate over all species is denoted as the black solid line.

including H_2^+, He^+, and Al^+. More specifically, H_2^+ and He^+ ions contribute at high altitude due to their extremely light mass while Al^+ contributes at high altitudes due to the high-temperature processes of MIV and charged-particle sputtering that underlie its neutral production. In comparison, at the subsolar point, panel 4(c), the maximum ion production rate is $\sim 1.5 \times 10^{-2}$ cm^{-3} s^{-1} and is dominated by CO^+ production. $^{40}Ar^+$ is the second most dominant species, followed by Ne^+, C^+, and O^+. Note that the C^+ and O^+ production at the subsolar point is dominated by photodissociative ionization of CO rather than ionization of atomic C and O.

Figure 5a shows the spatial distribution of the total pickup ion flux distribution in near-lunar space for standard solar wind conditions (v_{sw} = 425 km/s, $|B|$ = 5 nT), now displayed in the Solar-Selenocentric-Electric (SS-El) frame. In the SS-El frame, the $+x$ axis points antisunward and is nearly aligned with the solar wind flow vector, $\mathbf{V}$ (we neglect the small aberrative offset of the solar wind velocity, which Harada et al. (2015) have shown to produce a negligible effect on the compiled ARTEMIS data). The $+z$ axis is aligned with the vector given by $-\hat{\mathbf{x}} \times \hat{\mathbf{B}}$, where $\hat{\mathbf{B}}$ is the unit vector in the direction of the IMF. The $+y$ axis completes the right-handed set. In this coordinate system, the $+x$ axis is nearly coaligned with the solar wind velocity, $\mathbf{V}$, so for clarity, we label the $+x$ axis as $\hat{V}$. By extension, this also implies that the $+z$ axis in the SS-El frame is nearly along the convection electric field, $\mathbf{E}_c$, so we denote the $+z$ axis as $\hat{E}$. The dominant feature in the pickup ion flux distribution is a narrow plume of pickup ions with fluxes $\sim 10^6$ cm^{-2} s^{-1} originating from the lunar subsolar point and extending into the $+\hat{E}$ hemisphere. This plume is primarily composed of heavier species whose gyroradii are several tens of lunar radii (e.g., the heaviest species modeled here, Fe^+, has a gyroradius of ~29 lunar radii for the chosen solar wind conditions). At distances >~5 lunar radii, this plume begins to separate into several distinct plumes, as the divergence in gyroradii begins to take effect for ions of varying masses. Other distinct features include the cycloidal pickup trajectories for the two lightest species, H_2^+ and He^+, which have gyroradii of approximately 1.0 and 2.0 lunar radii, respectively, for the selected conditions. The H_2^+ ions undergo approximately two full gyrations downstream of the Moon before exiting the simulation domain, while the He^+ ions complete slightly less than one full gyration. The H_2^+ pickup ions can also be seen originating from both the $-\hat{E}$ and $+\hat{E}$ hemispheres of the Moon, yielding two distinct H_2^+ cycloids. The H_2^+ cycloid originating from the $-\hat{E}$ hemisphere is located almost entirely inside the lunar optical shadow and plasma wake. Distortions to the interplanetary magnetic field and/or the presence of electrostatic fields in the lunar wake (e.g., Halekas, Brain, & Holmström, 2014; Holmström et al., 2012; Xu et al., 2019) may alter the exact trajectories of these H_2^+ ions (and by extension, other species that transit through the wake); however, a detailed investigation of this possible effect is left for future work that utilizes three-dimensional plasma simulations for the lunar plasma environment.

In panel 5(b), we show a breakdown of the contribution of each species to the total pickup ion flux at four locations, denoted by the points in panel 5(a). These locations were selected to demonstrate the diversity and sensitivity of pickup ion fluxes to an observer's location in near-lunar space. Point 1 is located at an altitude of ~7 lunar radii directly within the densest portion of the lunar pickup ion plume. As such, pickup ion fluxes at Point 1 contain a broad mix of species but are generally dominated by CO^+ and Al^+, with additional contributions from Si^+, C^+, O^+, K^+, $^{40}Ar^+$, and Ca^+. Some of the lightest species, including He^+ and CH_4^+, contribute little to no flux at Point 1 as they cannot access Point 1's lateral distance due to their relatively smaller gyroradii and/or scale heights. Point 2 is located immediately above

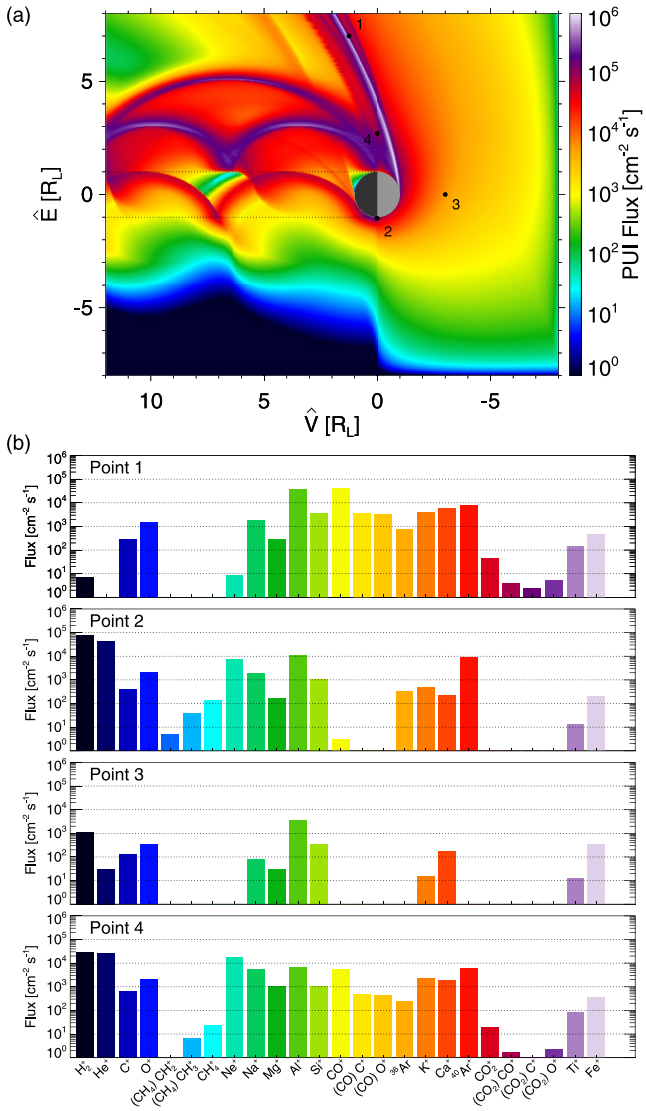

Figure 5. (a) The spatial distribution of the total pickup ion flux summed over all species in the lunar equatorial plane. (b) The distribution of ion species contributing to the pickup ion flux at the four respective points denoted in panel (a).

the lunar terminator on the $-\hat{E}$ hemisphere. Here, pickup ions are briefly accelerated in the solar wind electric field before impacting the lunar surface. At this location, the dominant species impacting the lunar surface are H_2^+ and He^+, with additional contributions from $^{40}Ar^+$ and Al^+; however, a broad mix of almost all other species are present as well. CO^+ ions are present at a very low level of flux while CO_2^+ ions (and related photodissociative products) are not present at levels higher than $\sim 10^0$ cm^{-2} s^{-1}.

Point 3 is located three lunar radii directly above the lunar subsolar point. At this altitude, the pickup ion flux is approximately two orders of magnitude less than at Point 1 and only species with very large scale heights are present, such as H_2^+, Al^+, O^+, C^+, and Si^+. In particular, none of the carbon-bearing species (CH_4^+, CO^+, and CO_2^+) nor either of the argon isotopes are detectable at Point 3, again it is due to their relatively smaller scale heights. Furthermore, the distribution of species seen at Point 3 is broadly applicable to all high-altitude locations above the Moon not located within the main pickup ion plume (cf., Point 1). Finally, Point 4 is placed at an altitude of 2.7 lunar radii above the $+\hat{E}$ lunar terminator, near to but slightly offset from the peak of the main pickup ion plume (at least for the median solar wind conditions used here). This location approximates the periselene location of the NASA Lunar Gateway station under the conditions where the interplanetary convection electric field satisfies $E_z > 0$. Similar to Point 1, a broad range of species contributes to the pickup ion flux at Point 4, with dominant contributions from H_2^+, He^+, Ne^+, Al^+, Na^+, CO^+, $^{40}Ar^+$, O^+, and K^+. In contrast to Point 1, however, pickup ion fluxes at Point 4 also contain contributions from several colder and/or lighter mass species, such as CH_4^+ and CO_2^+. Point 4 is located close enough to the Moon to encounter these species before their cycloidal trajectories bend significantly and fully separate from the densest part of the plume.

We also present results for the surface-sputtered ions in comparison with pickup ions generated from the exosphere. Of the eight species for which we included surface-sputtered ions (Na^+, Mg^+, Al^+, Si^+, K^+, Ca^+, Ti^+, and Fe^+) only Mg^+, Ca^+, and Ti^+ had surface-sputtered ion fluxes significantly larger than their corresponding fluxes of exospheric pickup ions. As an example, Figures 6a–6c shows a comparison of the exospheric, surface-sputtered, and total pickup ion flux for Ca^+ pickup ions, respectively. For the exospheric contribution, panel 6(a), the Ca^+ pickup ion flux distribution is broad and originates from both the dawn and dusk hemispheres, as well as the dayside and nightside hemispheres due to production via both charged-particle sputtering and MIV. Similar to that seen in the total pickup ion flux over all species shown in Figure 5a, the peak exospheric pickup ion flux occurs along a cycloidal ridge originating from the subsolar point. In comparison, the surface-sputtered Ca^+ pickup ion flux, panel 6(b), originates only from the dayside, $+\hat{E}$ hemisphere of the Moon. Surface-sputtered ions generated on the $-\hat{E}$ hemisphere of the Moon are immediately accelerated into the lunar regolith and recycled. The surface-sputtered pickup ions that do escape from the $+\hat{E}$ hemisphere of the Moon form a narrow and concentrated plume as the ions are accelerated by the interplanetary electric field. In total, the summed Ca^+ pickup ion distribution shown in panel 6(c) generally mirrors the exospheric pickup ion distribution in shape, with an additional enhancement along the peak pickup ion plume where the surface-sputtered ions overlap the exospheric distributions. For Ca^+ ions, the surface-sputtered ions in the plume are a factor of ~40 greater than the exospheric pickup ions. Similar to Mg^+, Ca^+, and Ti^+ surface-sputtered ions have maximum fluxes that are ~5, ~3, and ~2 times their maximum exospheric pickup ion flux, respectively, while Si^+ and Fe^+ surface-sputtered ions are both only ~30% their exospheric pickup ion flux. The Na^+, Al^+, and K^+ surface-sputtered ion fluxes were negligible compared to exospheric pickup ion fluxes.

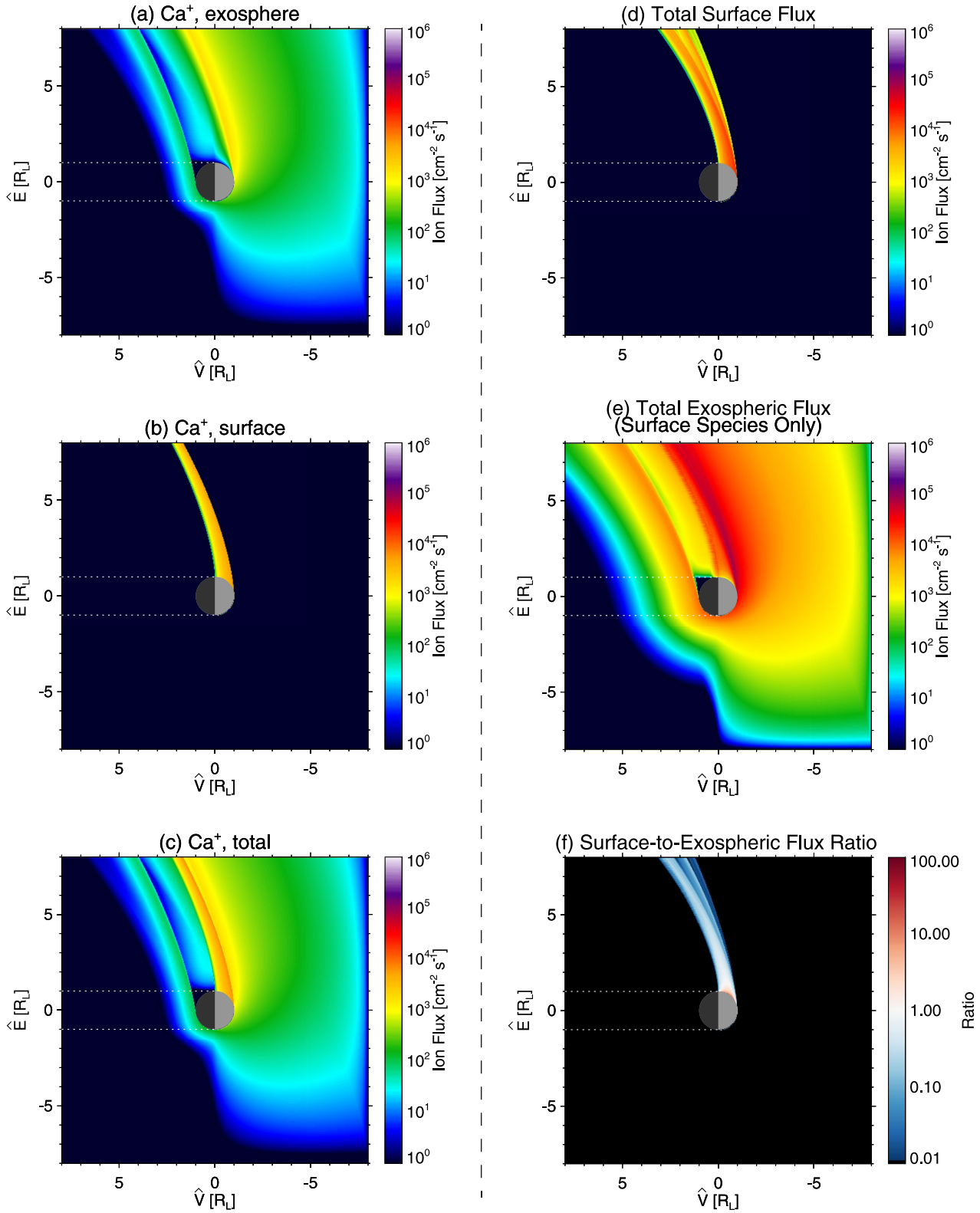

Figure 6. (a–c) The exospheric, surface-sputtered, and total pickup ion flux of Ca^+ ions, respectively. (d and e) The total surface-sputtered flux and exospheric flux for all eight neutral species with surface-sputtered fluxes. (f) The ratio of the surface-sputtered to exospheric pickup ion flux.

Summed together, we compare the total surface-sputtered flux to the total exospheric flux for the eight species generated via surface sputtering. Panel 6(d) shows the total surface-sputtered ion flux summed over all eight species. The total surface-sputtered flux is concentrated in a cycloidal plume similar to the results for Ca^+ ions only as shown in panel 6(b). At larger distances from the lunar surface (>~3 R_L), the plume begins to separate into several individual beams as the cycloidal pickup trajectories for different mass ions begin to diverge. The peak of the total surface-sputtered flux occurs at low altitudes above the lunar subsolar point with fluxes of ~2×10^4 cm^{-2} s^{-1}. In comparison, panel 6(e) shows the total exospheric pickup ion flux for the same eight species summed in panel 6(d). The total exospheric pickup ion flux peaks in a narrow plume originating from the lunar subsolar point similar to the surface-sputtered pickup ions but also possesses a broad, extended region of flux originating from hot and spatially extended neutral distributions. As shown in panel 6(f), the ratio of the surface-sputtered pickup ion flux to the exospheric pickup ion flux demonstrates that at very low altitudes (i.e., <~0.5 R_L) above the $+\hat{E}$ hemisphere of the dayside lunar surface, the surface-sputtered pickup ion flux can exceed the corresponding exospheric flux of surface-sputtered species by a factor of ~50. At larger distances along the pickup ion plume, however, the ratio decreases below unity as the increasing column of ionized exospheric pickup ions outweighs the surface-sputtered source of ions. At the end of the simulation domain at 8 R_L, the ratio is only ~0.2, indicating that the surface-sputtered ions are only a minor, although not entirely negligible, contribution to the overall ion flux.

4. Comparison to ARTEMIS Observations

4.1. ARTEMIS Observations and Data Reduction

We now compare the pickup ion model to in situ observations of lunar pickup ions by the ARTEMIS mission (Angelopoulos et al., 2008; Angelopoulos, 2011) in order to validate the model's large-scale predictions for lunar pickup ion fluxes. The ARTEMIS mission consists of a pair of identical probes in orbit around the Moon since mid-2011. Both probes are in highly elliptical orbits with periselenes varying between ~20 and 1000 km above the lunar surface and aposelenes between ~10 and 12 lunar radii. Each probe carries an extensive suite of fields and particle instruments; for our studies here, we make use of the ElectroStatic Analyzer (ESA; McFadden, Carlson, Larson, Ludlam, et al., 2008; McFadden, Carlson, Larson, Bonnell, et al., 2008) and the Fluxgate Magnetometer (FGM; Auster et al., 2008). The ESA instrument measures the three-dimensional distribution of ions and electrons at energies between ~5 and 25,000 eV at a maximum time resolution of once per spacecraft spin period (~4 s). We use the ESA "full" ion data set, which provides an ion velocity distribution with 32 energies and 88 solid angles at varying time resolutions. The FGM survey products provide the three-dimensional vector of the interplanetary magnetic field tied to the same cadence of the ESA particle distributions.

To calculate the average distribution of lunar pickup ions as observed by ARTEMIS, we followed the methodology outlined in Harada et al. (2015), which previously investigated the statistical distribution of near-lunar particle and wave distributions observed by ARTEMIS. The data reduction first restricted all observations to be in solar wind by specifying that the lunar position satisfied $X_{GSE} > 0$, where GSE is the Geocentric-Solar-Equatorial coordinate system. Next, the core solar wind population was removed from the data sets of both probes by eliminating all ions that have (a) energy-per-charge in the range $0.4E_{sw}/e < E/q < 4E_{sw}/e$, where $E_{sw}/e = 0.5m_p v_{sw}$ is the solar wind proton energy-per-charge, m_p is the proton mass, and v_{sw} is the bulk solar wind speed and (b) velocity vectors within 45° of the solar wind velocity. Finally, other heliospheric and/or nonlunar related phenomena (e.g., solar energetic particles and back-streaming terrestrial foreshock ions) were eliminated from the data sets at each probe by subtracting observations of one probe from the other probe and vice versa. We eliminated all data from this step that occurred when the reference probe (i.e., the probe whose data set is subtracted) was located within the lunar plasma wake. As discussed in Harada et al. (2015), this method can successfully subtract solar wind and/or heliospheric disturbances, leaving only lunar-related ion distributions. Harada et al. (2015) did note that this process can inadvertently subtract lunar-related phenomena if such phenomena occur simultaneously in both probes. Despite this, the ARTEMIS probes spend a majority of their time at large distances from the Moon due to their highly elliptical orbits, and thus the fraction of lunar-related particle fluxes that are potentially lost via this assumption is deemed negligible. The data set was also restricted to observations within ±0.5 R_L in the direction perpendicular to both $\hat{E}$ and $\hat{V}$. Additionally, all ARTEMIS observations are naturally restricted to ion energies, $E < 25$ keV, due to the upper energy limit of the ESA instrument (McFadden, Carlson, Larson, Ludlam,

et al., 2008). The previous results from Harada et al. (2015) covered July 2011 to December 2014; here, we have extended this data set to span from July 2011 to December 2021.

The left column of Figure 7 shows the ARTEMIS observations of nonsolar wind ions as compiled via the process described above. In panel 7(a), we present the spatial distribution of all nonsolar wind ions in the SS-Electric coordinate frame (see description of the SS-El frame above in Section 3.2). Nonsolar wind ion fluxes are strongest immediately above the subsolar point and extend into both the $+\hat{E}$ and $+\hat{V}$ directions, although nonsolar wind ion fluxes do appear at low altitudes on the $-\hat{E}$ hemisphere. At higher altitudes in the $-\hat{E}$ hemisphere, nonsolar wind ion fluxes are negligible. Lunar-related fluxes at the subsolar point reach approximately 5×10^6 cm^{-2} s^{-1} or equivalently ~2.5% of the average incident solar wind flux. As the plume of nonsolar wind ions extends in the $+\hat{E}$ and downstream $\left(+\hat{V}\right)$ directions, the magnitude decreases as the ions diverge along separate trajectories. Based on previous observations, the fluxes shown in panel 7(a) contain both lunar pickup ions (e.g., Yokota et al., 2009; Halekas et al., 2012, 2013) and solar wind protons reflected from both the lunar surface (e.g., Lue et al., 2018; Saito et al., 2008) and lunar crustal magnetic anomalies (e.g., Lue et al., 2011; Poppe et al., 2017; Yokota, Saito, et al., 2014). With relatively smaller gyroradii, reflected solar wind protons cannot extend to large distances in the $+\hat{E}$ hemisphere, while heavier pickup ions with comparatively larger gyroradii should extend farther in the $+\hat{E}$ hemisphere.

To better isolate the contribution of exospheric lunar pickup ions from reflected solar wind protons, we impose two additional restrictions on the ARTEMIS nonsolar wind data set, similar to Harada et al. (2015). First, we restricted the nonsolar wind ion data set to only include those observations originating from the single solid-angle bin corresponding to the direction of the interplanetary convection electric field. With the ARTEMIS data products utilized for this study, the solid angle subtended by an individual angular bin ranges from 0.12 to 0.17 str (e.g., see Figure 5a, McFadden, Carlson, Larson, Ludlam, et al., 2008). This distribution is shown in panel 7(b) and is significantly narrower than the full nonsolar wind ion distribution shown in panel 7(a). Nearly all of the nonsolar wind ion flux extending along the $+\hat{E}$ flank of the lunar wake has been removed, indicating that those ions have generally smaller gyroradii. Such ions mainly include the reflected solar wind proton population but could also include some contribution from lighter mass lunar exospheric pickup ions such as H_2^+ and He^+. We also note that some of the nonsolar wind flux at low altitudes in the $-\hat{E}$ hemisphere is also reduced compared to the full nonsolar wind ion distribution. The flux that has been removed here is likely due to solar wind protons reflected and/or scattered in arbitrary directions with respect to the interplanetary electric field. Nevertheless, the plume of nonsolar wind ions extending to several lunar radii along the $+\hat{E}$ direction is still present, albeit slightly diminished compared to the full nonsolar wind ion distribution in panel 7(a).

Next, we further restricted the nonsolar wind data set to exclude energies, $E < 2$ keV, which should remove much of the lower energy-reflected solar wind proton population, although this does remove pickup ions at early stages in their acceleration. We note again that the upper limit of 25 keV is set to the maximum detectable ion energy with the ESA instrument (McFadden, Carlson, Larson, Ludlam, et al., 2008). This distribution is shown in panel 7(c) and is most likely to be comprised of lunar exospheric pickup ions. Here, the peak flux is reduced by approximately an order of magnitude with respect to the distributions shown in panels 7(a) and (b) and the spatial extent is far narrower. Ion fluxes originate primarily from the lunar subsolar point and travel in the $+\hat{E}$ direction to lateral distances >4 R_L with slight deflection in the $+\hat{V}$ direction. Such trajectories are broadly consistent with the behavior of high-mass lunar pickup ions being accelerated by the interplanetary electric field and beginning their cycloidal trajectories around the IMF. Meanwhile, essentially no flux above the ARTEMIS background level (~10^4 cm^{-2} s^{-1}) is seen on the $-\hat{E}$ or nightside hemispheres.

4.2. Model-Data Comparison

While the modeled pickup ion flux distributions presented in, for example, Figures 5 and 6 are for a single, specific set of solar wind and IMF conditions, the ARTEMIS data set described above is averaged over nearly a solar cycle's worth of variability. Furthermore, when rotated into the SS-Electric frame, the ARTEMIS nonsolar wind ion data set includes observations from both the dawn and dusk flanks of the Moon. Thus, to make a proper comparison, the pickup ion flux model must be run over a similar range of conditions and likewise averaged together. The solar wind conditions governing pickup ion dynamics can be parameterized by the pickup proton

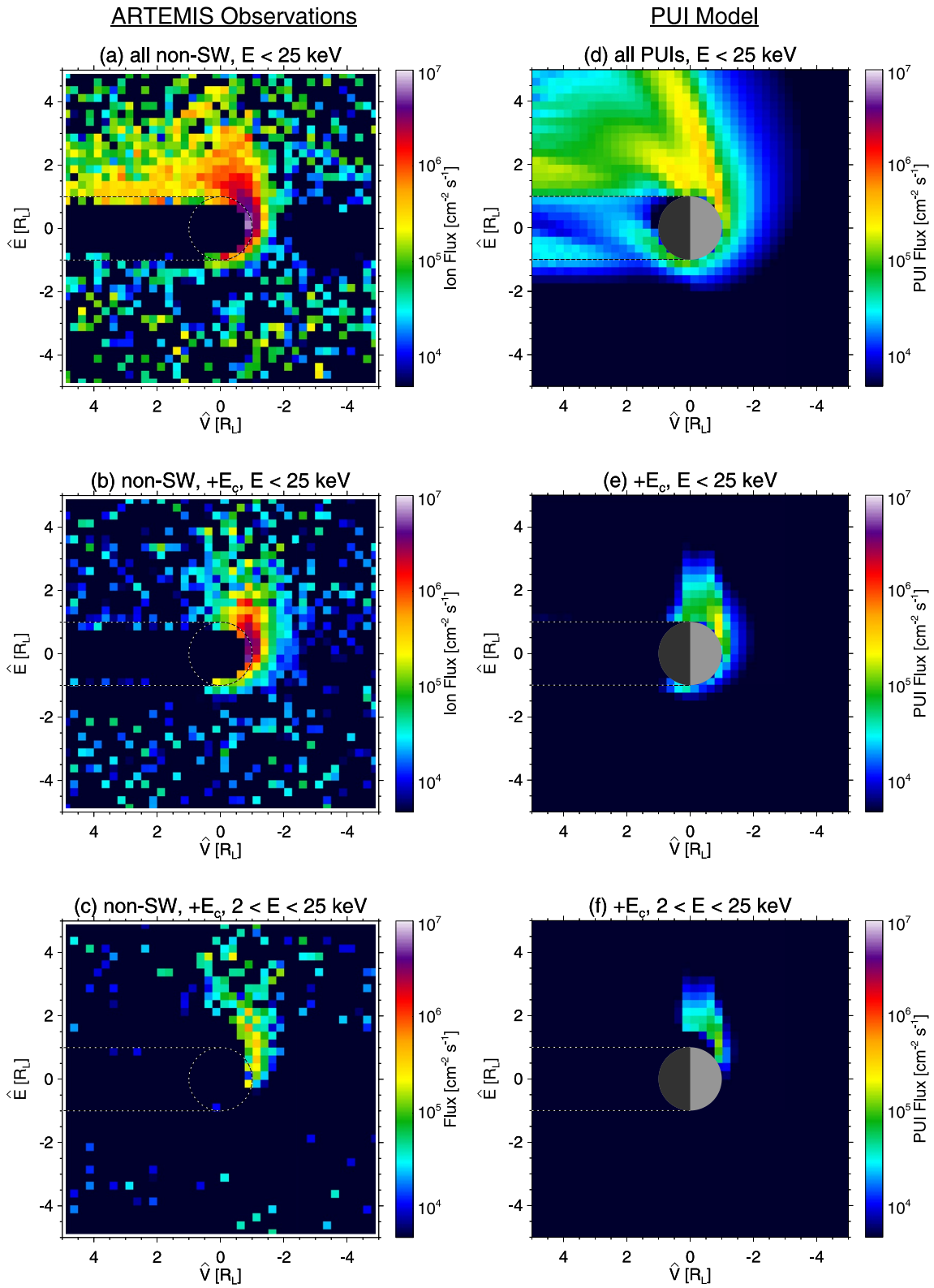

Figure 7. (left) ARTEMIS observations of nonsolar wind ions: (a) All nonsolar wind ions, (b) nonsolar wind ions aligned with the interplanetary convection electric field, and (c) nonsolar wind ions aligned with the interplanetary convection electric field and with energies between 2 and 25 keV (d–f) Average lunar pickup ion fluxes from the model for the same restrictions as panels (a–c), respectively.

gyroradius, $r_{g,p^+} = m_p v_\perp / e|B|$, where m_p and e are the proton mass and fundamental charge, respectively. We used the OMNI solar wind data set (King & Papitashvili, 2005) to extract the distribution of the solar wind perpendicular velocity, $v_\perp$, and the magnitude of the interplanetary magnetic field, $|B|$, over the same period used to compile the ARTEMIS data set (July 2011−December 2021). From these distributions, we then calculated the distribution of r_{g,p^+}, which was log-normally distributed with a peak at ∼650 km and a one-standard-deviation range of [380–1110] km (see Figure S1 in Supporting Information S1). We ran the pickup ion model for both dawnward and duskward interplanetary electric field configurations, respectively, for 20 distinct paired values of $[v_\perp, |B|]$ that spanned the full range of r_{g,p^+} calculated from the OMNI data set (see Figure S2 in Supporting Information S1). We then combined the resulting pickup ion flux distributions via a weighted average over the r_{g,p^+} distribution. Similar to the ARTEMIS data sets, we progressively filtered the model predictions in three steps: (a) All pickup ion flux with $E < 25$ keV (b) pickup ion fluxes within 12.5° (i.e., approximately one ARTEMIS ESA solid-angle bin), of the interplanetary electric field and $E < 25$ keV, and (c) pickup ion fluxes within 12.5° of the interplanetary electric field and with energies between 2 and 25 keV. Finally, we also down-resolved the pickup ion model results to a spatial resolution of 0.25×0.25 R_L and adjusted the range of displayed fluxes to match the ARTEMIS data set.

The right column of Figure 7 displays the modeled pickup ion fluxes as described in the previous paragraph. In panel 7(d), the modeled distribution for all pickup ion fluxes is primarily concentrated in a narrow plume originating from the lunar subsolar point and extending laterally from the Moon along the interplanetary electric field direction. Lower fluxes of $\sim 10^4 - 10^5$ cm^{-2} s^{-1} are present on the $-\hat{E}$ hemisphere of the Moon at low altitudes as well as through the lunar optical shadow and plasma wake. At this spatial resolution, the maximum modeled pickup ion fluxes are on the order of $\sim 3 \times 10^5$ cm^{-2} s^{-1}. In comparison to the ARTEMIS nonsolar wind fluxes shown in panel 7(a), the modeled pickup ion fluxes are approximately an order of magnitude less on the lunar dayside, at low lunar altitudes, and along the $+\hat{E}$ flank of the lunar optical shadow. As discussed previously, the large fluxes at low altitudes above the Moon and along the $+\hat{E}$ flank of the wake as observed by ARTEMIS are likely dominated by reflected solar wind protons. This is further supported by the absence of significant corresponding fluxes in the pickup ion model in these locations. Finally, there is some indication that at high altitudes (>∼1–2 R_L) above the lunar dayside surface, the modeled pickup ion flux is higher than the average ARTEMIS nonsolar wind distributions. The lack of higher altitude pickup ion fluxes in the ARTEMIS data suggests that the model is overestimating contributions from hotter, more spatially extended neutral distributions. This would primarily include contributions from charged-particle sputtering and MIV. On the other hand, the low levels of predicted ion fluxes at such high altitudes ($10^3 - 10^4$ cm^{-2} s^{-1}) are approaching the ARTEMIS ESA background level and thus this discrepancy may simply be due to the sensitivity limits of the instrumentation.

In panel 7(e), the modeled pickup fluxes restricted to those ions traveling within 12.5° of the interplanetary convection electric field are comprised of a plume of pickup ions originating from the lunar subsolar point extending in the $+\hat{E}$ direction. Lower magnitude fluxes are also present along the $-\hat{E}$ hemisphere of the Moon. The peak flux predicted by the model for this case is very slightly less than the peak flux considering all modeled pickup ions (i.e., panel 7(d)) but far less spatially extended. In comparison to the nonsolar wind ions observed by ARTEMIS in panel 7(b), the modeled pickup ions are located similarly but overall still less in magnitude by approximately an order of magnitude, especially at low altitudes. This suggests that reflected solar wind protons continue to contribute to the observed nonsolar wind ion flux at lower altitudes. At larger distances from the Moon, the plume of modeled pickup ion fluxes ceases at ∼3 R_L, whereas the nonsolar wind ions observed by ARTEMIS extend laterally to >4 R_L.

Finally, panels 7(f) and (c) compare the modeled pickup ion flux and the observed ARTEMIS nonsolar wind ion flux, subject to both restrictions of ions traveling within 12.5° of the interplanetary electric field and ions with energies between 2 and 25 keV. Similar to the comparison of just field-aligned ions in panels 7(b) and (e), the modeled pickup ion fluxes are less than the fluxes observed by ARTEMIS (by a factor of ∼3) and do not extend as far in the $+\hat{E}$ direction as the fluxes observed by ARTEMIS. As discussed in Harada et al. (2015), the simultaneous filters of field-aligned and >2 keV ions should eliminate nearly all the reflected proton populations, especially at larger distances from the Moon due to the relatively smaller proton gyroradii. Thus, the lower fluxes seen in the model for >2 keV, electric field-aligned conditions—especially at large distances from the Moon—suggest that the model is deficient in a heavy species that can extend in ionized form to large distances laterally from the Moon while maintaining a trajectory within 12.5° of $\hat{E}$. Based on the pickup ion gyroradius for typical

lunar conditions, we can estimate that the "missing" heavy species should have a mass, $m > \sim 20$ amu, in order to satisfy the $\hat{v} \cdot \hat{E} < 12.5°$ condition at distances >5 R_L from the Moon.

After a survey of possible missing or underestimated species in the model, we explored the possible contributions of two species to the modeled lunar exospheric pickup ion flux: H_2O and CO_2. As discussed in Section 2.1, we did not include a contribution from exospheric H_2O in the baseline model due to the lack of a definitive exospheric model; however, it nevertheless remains plausible that a steady-state water exosphere could be present at some level at the Moon. In comparison, we did include a CO_2 contribution to lunar pickup ion fluxes in the baseline model but with relatively small neutral densities of 125 cm^{-3} as constrained by the LADEE/NMS ion mode observations of Halekas et al. (2015) (in comparison, our modeled neutral density of CO peaks at 1.4×10^4 cm^{-3}). We suggest that the CO_2 exosphere could be underestimated despite its nondetection by LADEE/NMS. We quantified the possible effects of the inclusion of either an H_2O or a larger CO_2 exosphere on the magnitude and spatial distribution of lunar exospheric pickup ion fluxes. Specifically, we modeled a putative H_2O contribution as a thermal species (similar to H_2, He, and Ne) with subsolar densities of four values: 3.2×10^5, 1.0×10^6, 3.2×10^6, and 1.0×10^7 cm^{-3}. Separately, we modeled a CO_2 exosphere with four subsolar densities higher than our original value: 1.0×10^4, 3.2×10^4, 1.0×10^5, and 3.2×10^5 cm^{-3}. For each of these eight conditions, we added the additional hypothetical contribution (whether from H_2O or CO_2) to the baseline exospheric model (i.e., that presented in Figures 7d–7f) and recomputed the total modeled exospheric pickup ion flux.

Figure 8 shows the total high-energy, field-aligned pickup ion flux including (a–d) the four hypothetical neutral densities of H_2O and (e–h) the four hypothetical neutral densities of CO_2. In the case of H_2O, increased neutral densities yield corresponding increases in the magnitude of the modeled pickup ion flux; however, the spatial distribution of the total flux does not significantly change. In particular, the high-energy, field-aligned flux does not extend laterally beyond ~3 R_L. In comparison to the high-energy, field-aligned nonsolar wind ion flux observed by ARTEMIS as shown in panel 7(c), the inclusion of increased H_2O fluxes does not replicate the extended tail of pickup ions seen at relatively large lateral distances from the Moon, in agreement with our earlier estimation that the missing flux should originate from a species with $m > \sim 20$ amu. We do note that the ARTEMIS observations could be consistent with the inclusion of some level of H_2O, perhaps up to densities of $\sim 10^6$ cm^{-3}, without exceeding the observed magnitude of pickup ion fluxes; however, the data do not strictly require such a contribution. In the case of CO_2, the inclusion of higher neutral densities yields both an increase in the overall magnitude of the total high-energy, field-aligned pickup ion flux and an extension of pickup ion fluxes to increasing distances in the $+\hat{E}$ direction. By a simple visual comparison of the ARTEMIS observations in panel 7(c) and the various levels of additional CO_2 neutral densities, we qualitatively estimate that a subsolar neutral CO_2 density in the range of $[3.2 \times 10^4, 1 \times 10^5]$ is more consistent with the magnitude and spatial distribution of the observed pickup ion flux. We acknowledge that a CO_2 exosphere of such a relatively high density is in apparent conflict with the nondetection of CO_2^+ ions by LADEE/NMS (Halekas et al., 2015), which set an upper limit of $\sim 10^2$ cm^{-3}. Nevertheless, future measurements, either by in situ or remote-sensing instruments, should revisit the possible presence of CO_2 in the lunar exosphere to test our findings here.

5. Discussion and Conclusion

As demonstrated above, the lunar pickup ion environment is complex and multifaceted, reflecting the variety of physical mechanisms that operate on airless bodies in space. While some species are produced by a single source, for example, ^{40}Ar effusion from the lunar crust (Killen, 2002) or H_2 diffusion from implanted solar wind protons (Hurley et al., 2017; Tucker et al., 2019), species such as Na and K are produced by up to four separate mechanisms (thermal desorption, photon-stimulated desorption, solar wind sputtering, and MIV), yielding challenges in untangling the various sources. The wide range of characteristic source-process temperatures also contributes to a large dichotomy in the altitude profiles of the lunar pickup ion production rates (i.e., see Figure 4). Species emitted via thermal processes generally have much smaller scale heights (with the obvious exceptions of H_2 and He given their very light masses) while species emitted via more energetic processes maintain larger scale heights and, in some ways, may be more appropriately termed "coronae" as opposed to surface-boundary exospheres (e.g., Killen et al., 2018; Morgan & Killen, 1998). Indeed, evidence of such hot, high-altitude distributions in the lunar exosphere can be found in the analysis of ARTEMIS pickup ion observations (Halekas et al., 2016) and seen in the pickup ion model flux distributions shown here.

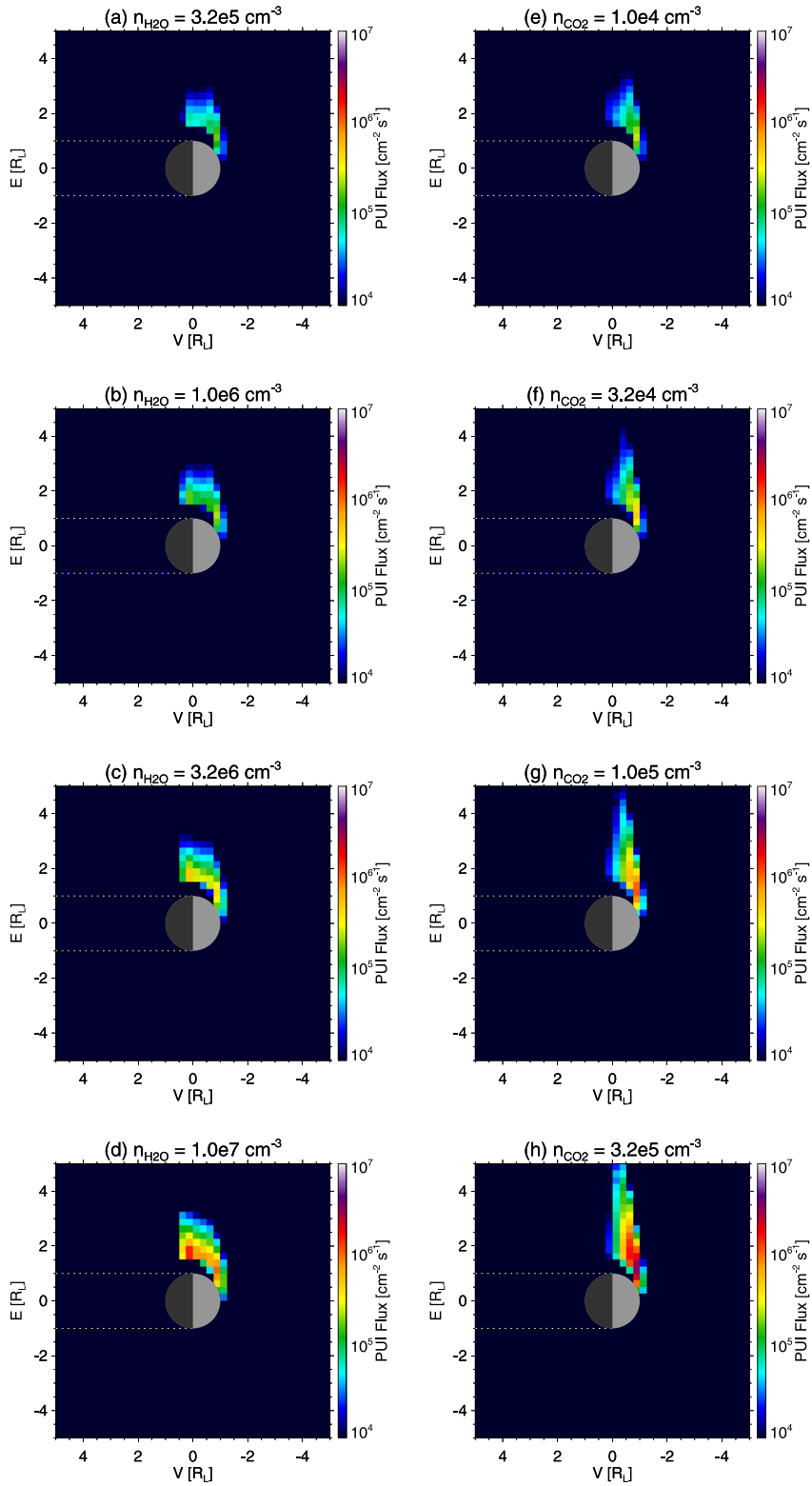

Figure 8. Total modeled lunar pickup ion fluxes aligned with the interplanetary convection electric field and with energies between 2 and 25 keV for (a–d) four hypothetical neutral densities of H_2O and (e–h) four hypothetical neutral densities of CO_2.

Despite the presence of at least 18 identified or hypothesized constituents, the dominant modeled lunar pickup ion species at various observing locations around the Moon typically include CO^+, $^{40}Ar^+$, Al^+, Na^+, K^+, Si^+, Ca^+, and O^+. In comparison to the model, the lunar pickup ion observations by the Wind spacecraft downstream of the Moon in the solar wind (Mall et al., 1998) reported the largest peak near mass 16 amu (O^+) with a broader secondary peak spanning masses from ∼25 to 32 amu, which includes primarily Al^+, CO^+, and Si^+. Lower fluxes of pickup ions in the mass range of ∼18–25 amu are also reported, which include species such as Ne^+, Na^+, and Mg^+. Qualitatively speaking, these measurements agree well with the model although the strength of the O^+ peak in the Wind/STICS data is larger than what the model predicts relative to other species such as K^+, Si^+/CO^+, and $^{40}Ar^+$, even when accounting for the multiple production branches of O^+ from photodissociative ionization of CO and/or CO_2 neutral species. Similar to the discussion in Halekas et al. (2015), this may provide further evidence of a more significant CO and/or CO_2 neutral population at the Moon than currently appreciated. Additionally, the lack of $^{40}Ar^+$ detections in the Wind data set is somewhat puzzling, given the well-known presence of neutral ^{40}Ar in the lunar exosphere and its detection in ionized form by both LADEE/NMS (Halekas et al., 2015) and Kaguya (Saito et al., 2010). This may be attributable to variability in the neutral Ar population at the Moon as reported by Benna et al. (2015) and Kegerreis et al. (2017) or to variability in the ionization rates as discussed above.

As discussed in the model comparison with ARTEMIS observations (Section 4.2), the potential inclusion of a significant CO_2 neutral density population in the lunar exosphere has broader implications for our understanding of the influx and recycling of solar wind carbon. As described in Hodges (1976), the solar wind provides a steady-state influx of highly charged carbon ions to the lunar surface (e.g., Bochsler, 1987, 2000) that must be balanced by an equivalent loss of carbon atoms. As argued in Hodges (1976), the dominant loss process for solar wind carbon atoms at the Moon is through a neutral exosphere—specifically via ionization and pickup of C-bearing ions into the solar wind flow. To this end, Hodges (1976) modeled neutral exospheres for three carbon-bearing molecules, CH_4, CO, and CO_2, that would each individually account for the required solar wind carbon loss rate. At the lunar equator, the peak neutral densities for the CH_4, CO, and CO_2 exospheres were approximately 1.5×10^5, 3×10^5, and 5×10^5 cm^{-3}, respectively; however, the lunar exosphere likely contains a weighted mixture of these three model exospheres depending on the specific chemistry that solar wind carbon atoms undergo upon implantation into the lunar regolith (e.g., Bibring et al., 1974; Cadogan et al., 1971; Chang et al., 1973; Chang & Lennon, 1975; Pillinger & Eglington, 1977; Pillinger et al., 1977). In the post-LADEE era, high signal-to-noise measurements of the CH_4 and CO exospheric densities have been reported (Halekas et al., 2015; Hodges & Mahaffy, 2016), allowing us to reassess the balance of these three hypothetical exospheres. In particular, LADEE/NMS observed maximum daytime densities of CH_4 of approximately 500 cm^{-3} (allowing for some uncertainty when extrapolating from LADEE's altitude to the lunar surface). This represents only ≈0.33% of the modeled CH_4 exosphere in Hodges (1976), implying that CH_4 cannot account for the escape of solar wind carbon. Additionally, LADEE/NMS ion mode observations detected mass 28 amu ions, which, as discussed earlier, are likely to be dominated by CO^+ (as opposed to N_2^+ or Si^+). An estimated dayside neutral CO density of $\approx 1.4 \times 10^4$ cm^{-3} is consistent with the LADEE/NMS ion measurements and satisfies a previous upper limit from the Apollo 17 Ultraviolet Spectrometer (Feldman & Morrison, 1991). This observed CO density is only ∼5% of the exospheric CO density required to account for the total solar wind carbon escape as estimated by Hodges (1976). Finally, the CO_2 neutral distribution hypothesized in our model to account for the total pickup ion flux as observed by ARTEMIS could account for up to 20% of the necessary carbon escape rate. Thus, taken together, the CH_4, CO, and CO_2 neutral densities can account for approximately 25% of the total solar wind carbon escape from the Moon as calculated by Hodges (1976). This suggests that either the Hodges (1976) Monte Carlo models potentially overestimate the neutral densities required to balance the solar wind carbon influx or other loss mechanisms, such as burial in the lunar regolith or sequestration in lunar polar cold traps (e.g., Colaprete et al., 2010; Schörghofer et al., 2021), are more significant than previously appreciated. Nevertheless, it is worth noting that the CO_2 exosphere hypothesized here could in fact be the most abundant species in the lunar exosphere, surpassing the peak density of ^{40}Ar by up to a factor of ∼2.

Our model can also be compared and contrasted with previous modeling investigations of the lunar exosphere and pickup ion environment. Prior to the launch of the LADEE mission, Sarantos et al. (2012a) constructed a model for the lunar pickup ion environment consisting of 12 species, including He, C, O, K, S, Mg, Na, Si, Al, Ti, Ca, and Fe. Species such as H_2, Ne, ^{36}Ar, and ^{40}Ar were not included nor were carbon-bearing molecular species (CH_4, CO, and CO_2). Similar to our approach, each species was assigned a neutral distribution reflective of its

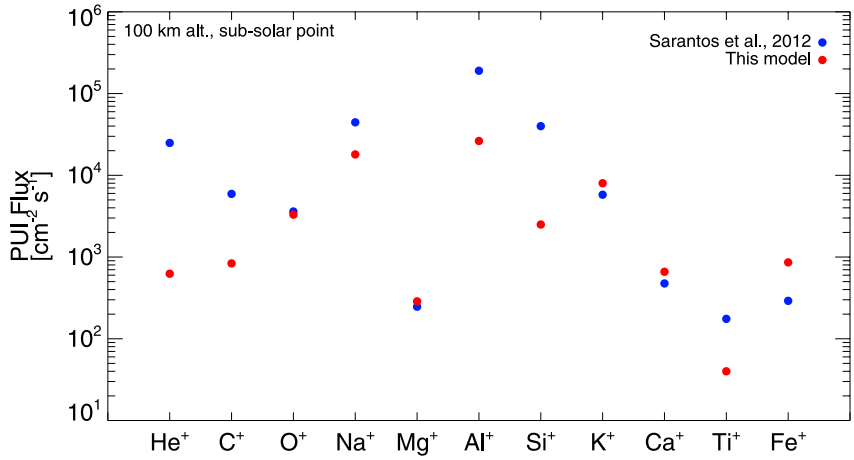

Figure 9. A comparison of pickup ion fluxes for 11 select species at 100 km above the lunar subsolar point between the model of Sarantos et al. (2012a) and the model presented here.

possible production mechanisms (e.g., thermal and/or photon-stimulated desorption, MIV, or charged-particle sputtering) and pickup ion fluxes calculated via an analytic approach. For the 11 species contained in both the Sarantos et al. (2012a) model and the model presented here (all species above except S), Figure 9 shows a comparison of the modeled pickup ion fluxes at 100 km altitude above the lunar subsolar point (see also Figure 2a of Sarantos et al. (2012a)). The modeled fluxes for many of these species are in agreement within better than a factor of five, including O^+, Na^+, Mg^+, K^+, Ca^+, Ti^+, and Fe^+, while the modeled fluxes for C^+ and Al^+ differ by factors of ∼7. These levels of differences can likely be attributed to different assumptions in the production rates of various mechanisms (e.g., charged-particle sputtering) and are likely well within the range of natural variability (e.g., the solar wind flux, which controls the rate of charged-particle sputtering, varies naturally by an order of magnitude). The greatest disagreement between the two models lies in the estimated He^+ and Si^+ fluxes, which are factors of ∼40 and ∼15 higher in the Sarantos et al. (2012a) model. Sarantos et al. (2012a) based their He^+ flux estimates on the work of Hartle and Thomas (1974), who in turn estimated He^+ fluxes using the simplifying assumption that all ions immediately assumed the solar wind drift speed, rather than slowly gaining velocity via the standard pickup process. This assumption may cause an overestimate in the flux for He^+, although we note that the exospheric neutral He densities vary by almost an order of magnitude due to variability in the incident solar wind alpha (He^{++}) flux (e.g., Benna et al., 2015; Bodmer et al., 1995; Cook & Stern, 2014; Feldman et al., 2012; Kasper et al., 2007). For Si^+, Poppe et al. (2016) found that neutral Si densities estimated in Sarantos et al. (2012b) produced excess high-altitude pickup ion flux as observed by the LADEE/Lunar Dust Experiment and recommended a reduction in modeled Si densities of ∼80%. Such a reduction in Si densities would also be closer in line with upper limits published by Cook et al. (2013) based on LRO/LAMP observations.

A more recent model of the lunar exosphere and ionosphere has been put forth by Choudhary et al. (2016) and Ambili and Choudhary (2022) in order to explain radio occultation measurements of a relatively dense ($n > 300$ cm^{-3}) lunar ionosphere by the Chandrayaan-1 radio occultation (RO) experiment. This model employs a fluid-based photochemical scheme to track the production and recombination of 16 separate ionized species, some of which overlap with the model presented here (specifically, CO_2, O, Ar, Ne, He, H_2, and CH_4). By matching the Chandrayaan-1 RO measurements (Choudhary et al., 2016), the model predicts the presence of a lunar ionosphere extending to altitudes >100 km at equatorial latitudes with densities >10^2 cm^{-3} even when accounting for the removal of lunar pickup ions by the solar wind convection electric field. On its face, such a dense ionosphere at these altitudes contradicts multiple in situ measurements of the lunar ionosphere, in particular measurements from the ARTEMIS probes within the solar wind (Harada et al., 2015; Zhang et al., 2014) or the terrestrial magnetotail (Halekas et al., 2018). As an example of such an in situ measurement, Figure 10 shows the nonsolar wind ion density observed by ARTEMIS, corresponding to the nonsolar wind ion flux shown in Figure 7a. The maximum nonsolar wind density peaks near the lunar subsolar point at densities of ∼0.1 cm^{-3} while decreasing along the pickup ion plume as the ions diverge away from the Moon. We do acknowledge that these in situ measurements from ARTEMIS are in tension with previous reports of a lunar ionosphere with

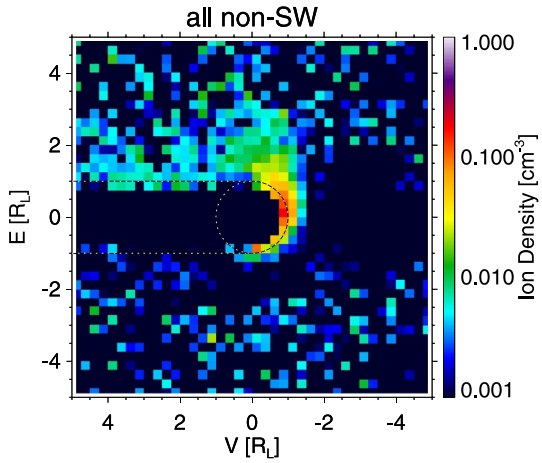

Figure 10. ARTEMIS observations of the nonsolar wind ion density in the solar-selenocentric-electric field frame.

densities on the order of hundreds per cm^{-3} (e.g., Choudhary et al., 2016; Imamura et al., 2012); however, a fuller exploration of this disagreement is left to future work, perhaps with further analysis of the ARTEMIS data set or with the aid of plasma measurements onboard in situ surface landers.

The lunar exosphere is also subject to a wide range of variability, present in both the source and loss rates. For source mechanisms, large degrees of variability are known to be or otherwise should be present in processes relating to solar wind or micrometeoroid influx (e.g., Wurz et al., 2022). Variability in the solar wind controls the delivery rate of protons and alpha particles that eventually neutralize and in the case of H, recombine into neutral H_2 and He, respectively (e.g., Benna et al., 2015; Cook & Stern, 2014; Hurley et al., 2017; Tucker et al., 2019). Charged-particle sputtering rates are also directly and promptly affected by changes in the incoming solar wind flux and alpha-to-proton ratio, including even "extreme" cases of sputtering rates during the passage of coronal mass ejections by the Moon (e.g., Killen et al., 2012). Passage of the Moon through the terrestrial magnetotail has been observed to broadly affect the production rates of multiple exospheric species (e.g., Killen et al., 2021; Potter et al., 2000; Sarantos et al., 2008; Wilson et al., 2006). Variability in the micrometeoroid influx to the Moon also has effects on the variation of neutral and ionized densities of species derived from micrometeoroid impact vaporization. The orbital motion of the Moon around the Earth and the seasonal motion of the Earth's orbit around the Sun both contribute to relatively longer period variation in the strength of MIV-produced species (e.g., Szalay & Horányi, 2015), while shorter period meteoroid showers at the Moon can temporarily increase the exospheric densities of such species (e.g., Hunten et al., 1998; Smith et al., 1999; Szalay et al., 2016; Verani et al., 1998). Finally, production rates of pickup ions (or equivalently, loss rates of exospheric neutral species) are also subject to variability. Changes in the solar irradiation at 1 au from both long-term, solar-cycle changes (e.g., Huang et al., 2016; Rottman, 1988) and short-term impulsive flares (e.g., Woods et al., 2004, 2011) readily alter photoionization rates, while changes in the solar wind parameters (e.g., density, speed, and electron temperature) alter the charge exchange and electron impact ionization rates of exospheric neutral species. Further studies with the pickup ion model presented here can explore the effects of these multiple sources of variability on the overall magnitude and spatial distribution of lunar pickup ions.

Looking forward, upcoming measurements of the lunar plasma environment by the SPAN-ion instrument onboard NASA's HERMES suite will provide deeper insight into the composition and variability of the lunar pickup ion population. The SPAN-ion instrument, identical to the similarly named instrument onboard the Parker Solar Probe spacecraft (Kasper et al., 2015), will enable energy-, angle-, and mass-resolved ion measurements along its proposed near-rectilinear halo orbit around the Moon. As currently envisioned, the HERMES periselene would be located above the lunar north pole at altitudes of ~3,000 km. Measurements of mass-resolved lunar pickup ion fluxes would strongly benefit from a configuration in which the SPAN-ion field of view included directions looking toward ecliptic south. In such a configuration, conditions under which the interplanetary convection electric field pointed northward (+z SSE) would accelerate lunar pickup ions into the SPAN-ion field of view while HERMES passed through periselene over the lunar north pole. Since +E_z conditions occur regularly due to the primarily in-ecliptic Parker Spiral configuration of the interplanetary magnetic field, HERMES/SPAN-ion would likely measure lunar pickup ion fluxes with relatively high probability. The mass resolution of the SPAN-ion instrument is variable with ion mass. At low masses, the instrument maintains $m/\Delta m$ values of 6.6 and 5.0 for H^+ and H_2^+ ions, respectively, sufficient for easily separating such species. At intermediate masses (e.g., C^+, N^+, and O^+) and higher, the mass resolution decreases and individual peaks begin to overlap in time-of-flight; however, ground-based calibrations will aid in fitting and isolating contributions from individual species (e.g., similar to the methodology used in the analysis of Kaguya Ion Mass Analyzer (IMA) data (e.g., Saito et al., 2010; Yokota et al., 2009, 2014a).

Data Availability Statement

The full ARTEMIS data set is publicly available at http://artemis.ssl.berkeley.edu or through NASA's CDAWeb tool (https://cdaweb.gsfc.nasa.gov/). Model results and the reduced ARTEMIS data presented in the manuscript are available at Poppe et al. (2022).

Acknowledgments
The authors gratefully acknowledge support from several sources that have contributed to the development of this model, including the NASA LASER program, grant #NNX13AJ97G, the NASA LADEE Guest Investigator program, grant #NNX14AR24G, the NASA SSERVI DREAM^2 team, grants #NNX14AG16A and #NNX15AH15A, the LEADER team, grant #80NSSC20M0060, the NASA LDAP program, grant #80NSSC20K0311, and the NASA ARTEMIS mission. We acknowledge NASA contract NAS5-02099 and V. Angelopoulos for use of data from the ARTEMIS Mission as well as J. P. McFadden and the late C. W. Carlson for use of ESA data, and K. H. Glassmeier, U. Auster, and W. Baumjohann for the use of FGM data provided under the lead of the Technical University of Braunschweig and with financial support through the German Ministry for Economy and Technology and the German Center for Aviation and Space (DLR) under contract 50 OC 0302. Finally, we thanks two anonymous reviewers for constructive comments that led to improvements in the manuscript.

References

Ambili, K. M., & Choudhary, R. K. (2022). Three-dimensional distribution of ions and electrons in the lunar ionosphere originated from the photochemical reactions. *Monthly Notices of the Royal Astronomical Society*, *510*(3), 3291–3300. https://doi.org/10.1093/mnras/stab3734

Angelopoulos, V. (2008). The THEMIS mission. *Space Science Reviews*, *141*(1–4), 5–34. https://doi.org/10.1007/s11214-008-9336-1

Angelopoulos, V. (2011). The ARTEMIS mission. *Space Science Reviews*, *165*(1–4), 3–25. https://doi.org/10.1007/s11214-010-9687-2

Auster, H. U., Glassmeier, K. H., Magnes, W., Aydogar, O., Baumjohann, W., Constantinescu, D., et al. (2008). The THEMIS fluxgate magnetometer. *Space Science Reviews*, *141*(1–4), 235–264. https://doi.org/10.1007/s11214-008-9365-9

Baragiola, R. A. (2004). Sputtering: Survey of observations and derived principles. *Philosophical Transactions of the Royal Society of London - A*, *362*(1814), 29–53. https://doi.org/10.1098/rsta.2003.1301

Baragiola, R. A., Atteberry, C. L., Dukes, C. A., Famá, M., & Teolis, B. D. (2002). Atomic collisions in solids: Astronomical applications. *Nuclear Instruments and Methods in Physics Research B*, *193*(1–4), 720–726. https://doi.org/10.1016/s0168-583x(02)00893-5

Barghouty, A. F., Meyer, F. W., Harris, P. R., & Adams, J. H., Jr. (2011). Solar-wind protons and heavy ion sputtering of lunar surface materials. *Nuclear Instruments and Methods B*, *269*(11), 1310–1315. https://doi.org/10.1016/j.nimb.2010.12.033

Behrisch, R., & Eckstein, W. (2007). Sputtering by particle bombardment: Experiments and computer calculations from threshold to MeV energies. In *Topics in applied physics* (Vol. 110). Springer Berlin Heidelberg.

Benna, M., Hurley, D. M., Stubbs, T. J., Mahaffy, P. R., & Elphic, R. C. (2019). Lunar soil hydration constrained by exospheric water liberated by meteoroid impacts. *Nature Geoscience*, *12*(5), 333–338. https://doi.org/10.1038/s41561-019-0345-3

Benna, M., Mahaffy, P. R., Halekas, J. S., Elphic, R. C., & Delory, G. T. (2015). Variability of helium, neon, and argon in the lunar exosphere as observed by the LADEE NMS instrument. *Geophysical Research Letters*, *42*(10), 3723–3729. https://doi.org/10.1002/2015gl064120

Berezhnoy, A. A. (2018). Chemistry of impact events on Mercury. *Icarus*, *300*, 210–222. https://doi.org/10.1016/j.icarus.2017.08.034

Berezhnoy, A. A., & Klumov, B. A. (2008). Impacts as sources of the exosphere on Mercury. *Icarus*, *195*(2), 511–522. https://doi.org/10.1016/j.icarus.2008.01.005

Bibring, J. P., Burlingame, A. L., Chaumont, J., Langevin, Y., Maurette, M., & Wszolek, P. C. (1974). Simulation of lunar carbon chemistry: I. Solar wind contribution. *Proceedings of the fifth Lunar Science Conference*, (Vol. *2*, pp. 1747–1762).

Biersack, J. P., & Eckstein, W. (1984). Sputtering studies with the Monte Carlo Program TRIM.SP. *Applied Physics A*, *34*(2), 73–94. https://doi.org/10.1007/bf00614759

Bochsler, P. (1987). Solar wind ion composition. *Physica Scripta*, *T18*, 55–60. https://doi.org/10.1088/0031-8949/1987/t18/007

Bochsler, P. (2000). Abundances and charge states of particles in the solar wind. *Reviews of Geophysics*, *38*(2), 247–266. https://doi.org/10.1029/1999rg000063

Bodmer, R., Bochsler, P., Geiss, J., von Steiger, R., & Gloeckler, G. (1995). Solar wind helium isotopic composition from SWICS/Ulysses. *Space Science Reviews*, *72*(1–2), 61–64. https://doi.org/10.1007/bf00768754

Bryant, D. A., Krimigis, S. M., & Haerendel, G. (1985). Outline of the Active Magnetospheric Particle tracer Explorers (AMPTE) mission. *IEEE Transactions on Geoscience and Remote Sensing*, *23*(3).

Butler, B. J. (1997). The migration of volatiles on the surfaces of Mercury and the Moon. *Journal of Geophysical Research*, *102*(E8), 19283–19291. https://doi.org/10.1029/97je01347

Cadogan, P. H., Eglington, G., Maxwell, J. R., & Pillinger, C. T. (1971). Carbon chemistry of the lunar surface. *Nature*, *231*(5297), 29–31. https://doi.org/10.1038/231029a0

Cao, X., Halekas, J., Poppe, A., Chu, F., & Glassmeier, K.-H. (2020). The acceleration of lunar ions by magnetic forces in the terrestrial magnetotail lobes. *Journal of Geophysical Research: Space Physics*, *125*(6). https://doi.org/10.1029/2020JA027829

Cao, X., Halekas, J. S., Chu, F., Kistler, M., Poppe, A. R., & Glassmeier, K.-H. (2020). Plasma convection in the terrestrial magnetotail lobes measured near the Moon's orbit. *Geophysical Research Letters*, *47*(20). https://doi.org/10.1029/2020GL090217

Cassidy, T. A., & Johnson, R. E. (2005). Monte Carlo model of sputtering and other ejection processes within a regolith. *Icarus*, *176*(2), 499–507. https://doi.org/10.1016/j.icarus.2005.02.013

Chang, S., & Lennon, K. (1975). Implantation of carbon and nitrogen ions into lunar fines: Trapping efficiencies and saturation concentrations. *Proceedings of the Lunar and Science Conference*, (Vol. *6*(6), pp. 2179–2188).

Chang, S., Mack, R., Gibson, E. K., Jr., & Moore, G. W. (1973). Simulated solar wind implantation of carbon and nitrogen ions into terrestrial basalt and lunar fines. *Proceedings of the 4th Lunar and Science Conference*, (Vol. *2*, pp. 1509–1522).

Choudhary, R., Ambili, K., Choudhury, S., Dhanya, M., & Bhardwaj, A. (2016). On the origin of the ionosphere at the moon using results from Chandrayaan-1 s band radio occultation experiment and a photochemical model. *Geophysical Research Letters*, *43*(19), 10–025. https://doi.org/10.1002/2016gl070612

Christon, S. P., Hamilton, D. C., Mitchell, D. G., Plane, J. M. C., & Nylund, S. R. (2020). Suprathermal magnetospheric atomic and molecular heavy ions at and near Earth, Jupiter, and Saturn: Observations and identification. *Journal of Geophysical Research: Space Physics*, *125*(1). https://doi.org/10.1029/2019JA027271

Cladis, J. B., Francis, W. E., & Vondrak, R. R. (1994). Transport toward Earth of ions sputtered from the Moon's surface by the solar wind. *Journal of Geophysical Research*, *99*(A1), 53–64. https://doi.org/10.1029/93ja02672

Clark, R. N. (2009). Detection of adsorbed water and hydroxyl on the Moon. *Science*, *326*(5952), 562–564. https://doi.org/10.1126/science.1178105

Colaprete, A., Schultz, P., Heldmann, J., Wooden, D., Shirley, M., Ennico, K., et al. (2010). Detection of water in the LCROSS Ejecta Plume. *Science*, *330*(463), 468. https://doi.org/10.1126/science.1186986

Collette, A., Drake, K., Mocker, A., Sternovsky, Z., Munsat, T., & Horányi, M. (2013). Time-resolved temperature measurements in hypervelocity dust impacts. *Planetary and Space Science*, *89*, 58–62. https://doi.org/10.1016/j.pss.2013.02.007

Collette, A., Sternovsky, Z., & Horányi, M. (2014). Production of neutral gas by micrometeoroid impacts. *Icarus*, *227*, 89–93. https://doi.org/10.1016/j.icarus.2013.09.009

Cook, J. C., & Stern, S. A. (2014). Sporadic increases in lunar atmospheric helium detected by LAMP. *Icarus*, *236*, 48–55. https://doi.org/10.1016/j.icarus.2014.02.001

Cook, J. C., Stern, S. A., Feldman, P. D., Gladstone, G. R., Retherford, K. D., & Tsang, C. C. C. (2013). New upper limits on numerous atmospheric species in the native lunar atmosphere. *Icarus*, *225*(1), 681–687. https://doi.org/10.1016/j.icarus.2013.04.010

Crider, D. H., & Vondrak, R. R. (2000). The solar wind as a possible source of lunar polar hydrogen deposits. *Journal of Geophysical Research*, *105*(E11), 773–782. https://doi.org/10.1029/2000je001277

Das, T. P., Thampi, S. V., Bhardwaj, A., Ahmed, S. M., & Sridharan, R. (2016). Observation of Neon at mid and high latitudes in the sunlit lunar exosphere: Results from CHACE aboard MIP/Chandrayaan-1. *Icarus*, *272*, 206–211. https://doi.org/10.1016/j.icarus.2016.02.030

Dmitriev, A. V., Suvorova, A. V., & Veselovsky, I. S. (2011). Statistical characteristics of the heliospheric plasma and magnetic field at Earth's orbit during four solar cycles 20-23. In H. E. Johannson (Ed.), *Handbook on solar wind: Effects, dynamics, and interactions* (pp. 81–144). NOVA Science Publishers. chap. 2.

Dukes, C. A., & Baragiola, R. A. (2015). The lunar surface-exosphere connection: Measurement of secondary ions from Apollo soils. *Icarus*, *255*, 51–57. https://doi.org/10.1016/j.icarus.2014.11.032

Dukes, C. A., Chang, W.-Y., Famá, M., & Baragiola, R. A. (2011). Laboratory studies on the sputtering contribution to the sodium atmospheres of Mercury and the Moon. *Icarus*, *212*(2), 463–469. https://doi.org/10.1016/j.icarus.2011.01.027

Eichhorn, G. (1976). Analysis of the hypervelocity impact process from impact flash measurements. *Planetary and Space Science*, *24*(8), 771–781. https://doi.org/10.1016/0032-0633(76)90114-8

Eichhorn, G. (1978). Heating and vaporization during hypervelocity particle impact. *Planetary and Space Science*, *26*(5), 463–467. https://doi.org/10.1016/0032-0633(78)90067-3

Elphic, R. C., Funsten, H. O., III, Barraclough, B. L., McComas, D. J., Paffett, M. T., Vaniman, D. T., & Heiken, G. (1991). Lunar surface composition and solar wind-induced secondary ion mass spectrometry. *Geophysical Research Letters*, *18*(11), 2165–2168. https://doi.org/10.1029/91gl02669

Eugster, O., Terribilini, D., Polnau, E., & Kramers, J. (2001). The antiquity indicator argon-40/argon-36 for lunar surface samples calibrated by uranium-235 − xenon136 dating. *Meteoritics & Planetary Science*, *36*(8), 1097–1115. https://doi.org/10.1111/j.1945-5100.2001.tb01947.x

Fagan, A. L., Joy, K. H., Bogard, D. D., & Kring, D. A. (2014). Ages of globally distributed lunar paleoregoliths and soils from 3.9 Ga to the Present. *Earth, Moon, and Planets*, *112*(1–4), 59–71. https://doi.org/10.1007/s11038-014-9437-7

Farrell, W. M., Poppe, A. R., Zimmerman, M. I., Halekas, J. S., Delory, G. T., & Killen, R. M. (2013). The lunar photoelectrons sheath: A change in trapping efficiency during a solar storm. *Journal of Geophysical Research: Planets*, *118*(5), 1114–1122. https://doi.org/10.1002/jgre.20086

Feldman, P. D., Hurley, D. M., Retherford, K. D., Gladstone, G. R., Stern, S. A., Pryor, W., & LAMP Team. (2012). Temporal variability of lunar exospheric helium during January 2012 from LRO/LAMP. *Icarus*, *221*(2), 854–858. https://doi.org/10.1016/j.icarus.2012.09.015

Feldman, P. D., & Morrison, D. (1991). The Apollo 17 ultraviolet spectrometer: Lunar atmosphere measurements revisited. *Geophysical Research Letters*, *18*(11), 2105–2109. https://doi.org/10.1029/91gl01998

Füri, E., Marty, B., & Assonov, S. S. (2012). Constraints on the flux of meteoritic and cometary water on the Moon from volatile element (N-Ar) analysis of single lunar soil grains, Luna 24 core. *Icarus*, *218*(1), 220–229. https://doi.org/10.1016/j.icarus.2011.11.037

Gamborino, D., & Wurz, P. (2018). Velocity distribution function of Na released by photons from planetary surfaces. *Planetary and Space Science*, *159*, 97–104. https://doi.org/10.1016/j.pss.2018.04.021Y

Grava, C., Chaufray, J.-Y., Retherford, K. D., Gladstone, G. R., Greathouse, T. K., Hurley, D. M., et al. (2015). Lunar exospheric argon modeling. *Icarus*, *255*, 135–147. https://doi.org/10.1016/j.icarus.2014.09.029

Grava, C., Hurley, D. M., Feldman, P. D., Retherford, K. D., Greathouse, T. K., Pryor, W. R., et al. (2021). LRO/LAMP observations of the lunar helium exosphere: Constraints on thermal accommodation and outgassing rate. *Monthly Notices of the Royal Astronomical Society*, *501*(3), 4438–4451. https://doi.org/10.1093/mnras/staa3884

Halekas, J. S., Benna, M., Mahaffy, P. R., Elphic, R. C., Poppe, A. R., & Delory, G. T. (2015). Detections of lunar exospheric ions by the LADEE neutral mass spectrometer. *Geophysical Research Letters*, *42*(13), 5162–5169. https://doi.org/10.1002/2015gl064746

Halekas, J. S., Brain, D. A., & Holmström, M. (2014). The Moon's plasma wake. In A. Keiling (Ed.), *Magnetotails in the solar system*. American Geophysical Union.

Halekas, J. S., Poppe, A. R., Delory, G. T., Sarantos, M., Farrell, W. M., Angelopoulos, V., & McFadden, J. P. (2012). Lunar pickup ions observed by ARTEMIS: Spatial and temporal distribution and constraints on species and source locations. *Journal of Geophysical Research*, *117*(E06006). https://doi.org/10.1029/2012je004107

Halekas, J. S., Poppe, A. R., Delory, G. T., Sarantos, M., & McFadden, J. P. (2013). Utilizing ARTEMIS pickup ion observations to place constraints on the lunar atmosphere. *Journal of Geophysical Research*, *118*, 1–8. https://doi.org/10.1029/2012je004292

Halekas, J. S., Poppe, A. R., Farrell, W. M., & McFadden, J. P. (2016). Structure and composition of the distant lunar exosphere: Constraints from ARTEMIS observations of ion acceleration in time-varying fields. *Journal of Geophysical Research: Planets*, *121*(6), 1102–1115. https://doi.org/10.1002/2016je005082

Halekas, J. S., Poppe, A. R., Harada, Y., Bonnell, J. W., Ergun, R. E., & McFadden, J. P. (2018). A tenuous lunar ionosphere in the geomagnetic tail. *Geophysical Research Letters*, *45*(18), 9450–9459. https://doi.org/10.1029/2018GL079936

Halekas, J. S., Poppe, A. R., Lue, C., Farrell, W. M., & McFadden, J. P. (2017). Distribution and solar wind control of compressional solar wind-magnetic anomaly interactions observed at the Moon by ARTEMIS. *Journal of Geophysical Research: Space Physics*, *122*(6), 6240–6254. https://doi.org/10.1002/2017ja023931

Halekas, J. S., Poppe, A. R., McFadden, J. P., Angelopoulos, V., Glassmeier, K.-H., & Brain, D. A. (2014). Evidence for small-scale collisionless shocks at the Moon from ARTEMIS. *Geophysical Research Letters*, *41*(21), 7436–7443. https://doi.org/10.1002/2014gl061973

Harada, Y., Halekas, J. S., Poppe, A. R., Tsugawa, Y., Kurita, S., & McFadden, J. P. (2015). Statistical characterization of the foremoon particle and wave morphology: ARTEMIS observations. *Journal of Geophysical Research: Space Physics*, *120*(6), 4907–4921. https://doi.org/10.1002/2015ja021211

Hartle, R. E., & Killen, R. (2006). Measuring pickup ions to characterize the surfaces and exospheres of planetary bodies: Applications to the Moon. *Geophysical Research Letters*, *33*(5), L05201. https://doi.org/10.1029/2005gl024520

Hartle, R. E., & Thomas, G. E. (1974). Neutral and ion Exosphere models for lunar hydrogen and helium. *Journal of Geophysical Research*, *79*(10), 1519–1526. https://doi.org/10.1029/JA079i010p01519

Hijazi, H., Bannister, M. E., Meyer, H. M., III, Rouleau, C. M., Barghouty, A. F., Rickman, D. L., & Meyer, F. W. (2014). Anorthite sputtering by H^+ and Ar^{q+} ($q = 1 - 9$) at solar wind velocities. *Journal of Geophysical Research: Space Physics*, *119*(10), 8006–8016. https://doi.org/10.1002/2014ja020140

Hilchenbach, M., Hovestadt, D., Klecker, B., & Möbius, E. (1993). Observations of energetic lunar pick-up ions near Earth. *Advances in Space Research*, *13*(10), 321–324. https://doi.org/10.1016/0273-1177(93)90086-q

Hodges, R. R. (1975). Formation of the lunar atmosphere. *The Moon*, *14*(1), 139–157. https://doi.org/10.1007/bf00562980
Hodges, R. R. (1976). The escape of solar-wind carbon from the moon. *Proceedings of the Lunar Science and Conference*, (Vol. *7*, pp. 493–500).
Hodges, R. R. (1980). Lunar cold traps and their influence on argon-40. *Proceedings of the Lunar and Planetary Science Conference*, (Vol. *11th*(11), pp. 2463–2477).
Hodges, R. R. (1991). Exospheric transport restrictions on water ice in lunar polar traps. *Geophysical Research Letters*, *18*(11), 2113–2116. https://doi.org/10.1029/91gl02533
Hodges, R. R. (2016). Methane in the lunar exosphere: Implications for solar wind carbon escape. *Geophysical Research Letters*, *43*(13), 6742–6748. https://doi.org/10.1002/2016GL068994
Hodges, R. R., & Hoffman, J. H. (1975). Implications of atmospheric ^{40}Ar escape on the interior structure of the Moon. *Proceedings of the Lunar and Planetary Science Conference*, (Vol. *6*, pp. 3039–3047).
Hodges, R. R., Hoffman, J. H., & Johnson, F. S. (1974). The lunar atmosphere. *Icarus*, *21*(4), 415–426. https://doi.org/10.1016/0019-1035(74)90144-4
Hodges, R. R., Hoffman, J. H., Johnson, F. S., & Evans, D. E. (1973). Composition and dynamics of lunar atmosphere. *Proceedings of the 4th Lunar and Planetary Science Conference*, (Vol. *3*, pp. 2855–2864).
Hodges, R. R., & Johnson, F. S. (1968). Lateral transport in planetary exospheres. *Journal of Geophysical Research*, *73*(23), 7307–7317. https://doi.org/10.1029/ja073i023p07307
Hodges, R. R., & Mahaffy, P. R. (2016). Synodic and semiannual oscillations of argon-40 in the lunar exosphere. *Geophysical Research Letters*, *43*(1), 22–27. https://doi.org/10.1002/2015gl067293
Hoffman, J. H., & Hodges, R. R. (1975). Molecular gas species in the lunar atmosphere. *The Moon*, *14*(1), 159–167. https://doi.org/10.1007/bf00562981
Hoffman, J. H., Hodges, R. R., Jr., Johnson, F. S., & Evans, D. E. (1973). Lunar atmospheric composition results from Apollo 17. *Proceedings of the 4th Lunar and Planetary Science Conference*,(Vol. *3*, pp. 2865–287).
Holmström, M., Fatemi, S., Futaana, Y., & Nilsson, H. (2012). The interaction between the Moon and the solar wind. *Earth Planets and Space*, *64*(2), 237–245. https://doi.org/10.5047/eps.2011.06.040
Honniball, C. I., Lucey, P. G., Li, S., Shenoy, S., Orlando, T. M., Hibbits, C. A., et al. (2021). Molecular water detected on the sunlit Moon by SOFIA. *Nature Astronomy*, *5*(2), 121–127. https://doi.org/10.1038/s41550-020-01222-x
Horányi, M., Szalay, J. R., Kempf, S., Schmidt, J., Grün, E., Srama, R., & Sternovsky, Z. (2015). A permanent, asymmetric dust cloud around the Moon. *Nature*, *522*(7556), 324–326. https://doi.org/10.1038/nature14479
Huang, J., Hao, Y., Zhang, D., & Xiao, Z. (2016). Changes of solar extreme ultraviolet spectrum in solar cycle 24. *Journal of Geophysical Research: Space Physics*, *121*(7), 6844–6854. https://doi.org/10.1002/2015JA022231
Huebner, W. F., & Mukherjee, J. (2015). Photoionization and photodissociation rates in solar and blackbody radiation fields. *Planetary and Space Science*, *106*, 11–45. https://doi.org/10.1016/j.pss.2014.11.022
Hunten, D. M., Cremonese, G., Sprague, A. L., Hill, R. E., Verani, S., & Kozlowski, R. W. H. (1998). The Leonid meteor shower and the lunar sodium atmosphere. *Icarus*, *136*(2), 298–303. https://doi.org/10.1006/icar.1998.6023
Hurley, D. M., & Benna, M. (2018). Simulations of lunar exospheric water events from meteoroid impacts. *Planetary and Space Science*, *162*, 148–156. https://doi.org/10.1016/j.pss.2017.07.008
Hurley, D. M., Cook, J. C., Benna, M., Halekas, J. S., Feldman, P. D., Retherford, K. D., et al. (2016). Understanding temporal and spatial variability of the lunar helium atmosphere using simultaneous observations from LRO, LADEE, and ARTEMIS. *Icarus*, *273*, 45–52. https://doi.org/10.1016/j.icarus.2015.09.011
Hurley, D. M., Cook, J. C., Retherford, K. D., Greathouse, T., Gladstone, G. R., Mandt, K., et al. (2017). Contributions of solar wind and micrometeoroids to molecular hydrogen in the lunar exosphere. *Icarus*, *283*, 31–37. https://doi.org/10.1016/j.icarus.2016.04.019
Hurley, D. M., Sarantos, M., Grava, C., Williams, J.-P., Retherford, K. D., Siegler, M., et al. (2015). An analytic function of lunar surface temperature for exospheric modeling. *Icarus*, *255*, 159–163. https://doi.org/10.1016/j.icarus.2014.08.043
Husinsky, W., Girgis, I., & Betz, G. (1985). Doppler shift laser fluorescence spectroscopy of sputtered and evaporated atoms under Ar^+ bombardment. *Journal of Vacuum Science and Technology B*, *3*(5), 1543–1545. https://doi.org/10.1116/1.582982
Imamura, T., Nabatov, A., Mochizuki, N., Iwata, T., Hanada, H., Matsumoto, K., et al. (2012). Radio occultation measurement of the electron density near the lunar surface using a subsatellite on the SELENE mission. *Journal of Geophysical Research*, *117*(A06303). https://doi.org/10.1029/2011ja017293
Ip, W.-H. (1991). The atomic sodium exosphere/coma of the Moon. *Geophysical Research Letters*, *18*(11), 2093–2096. https://doi.org/10.1029/91gl02549
Janches, D., Berezhnoy, A. A., Christou, A. A., Cremonese, G., Hirai, T., Horányi, M., et al. (2021). Meteoroids as one of the sources for Exosphere formation on airless bodies in the inner solar system. *Space Science Reviews*, *217*(50). https://doi.org/10.1007/s11214-021-00827-6
Janches, D., Pokorný, P., Sarantos, M., Szalay, J. R., Horányi, M., & Nesvorný, D. (2018). Constraining the ratio of micrometeoroids from short- and long-Period Comets at 1 AU from LADEE observations of the lunar dust cloud. *Geophysical Research Letters*, *45*(4), 1713–1722. https://doi.org/10.1002/2017GL076065
Johnson, R. E., & Baragiola, R. (1991). Lunar surface: Sputtering and secondary ion mass spectrometry. *Geophysical Research Letters*, *18*(11), 2169–2172. https://doi.org/10.1029/91gl02095
Johnson, R. E., & Leblanc, F. (2001). The physics and chemistry of sputtering by energetic plasma ions. *Astrophysics and Space Science*, *277*(1/2), 259–269. https://doi.org/10.1023/a:1012257024699
Kasper, J. C., Abiad, R., Austin, G., Balat-Pichelin, M., Bale, S. D., Belcher, J. W., et al. (2015). Solar Wind Electrons Alphas and Protons (SWEAP) investigation: Design of the solar wind and coronal plasma instrument suite for solar probe plus. *Space Science Reviews*(1–4), 131–186. https://doi.org/10.1007/s11214-015-0206-3
Kasper, J. C., Stevens, M. L., Lazarus, A. J., Steinberg, J. T., & Ogilvie, K. W. (2007). Solar wind helium abundance as a function of speed and heliographic latitude: Variation through a solar cycle. *The Astrophysical Journal*, *660*(1), 901–910. https://doi.org/10.1086/510842
Kegerreis, J. A., Eke, V. R., Massey, R. J., Beaumont, S. K., Elphic, R. C., & Teodoro, L. F. (2017). Evidence for a Localised source of the argon in the lunar Exosphere. *Journal of Geophysical Research: Planets*, *122*(10), 2163–2181. https://doi.org/10.1002/2017je005352
Killen, R. M. (2002). Source and maintenance of the argon atmospheres of Mercury and the Moon. *Meteoritics & Planetary Science*, *37*(9), 1223–1231. https://doi.org/10.1111/j.1945-5100.2002.tb00891.x
Killen, R. M. (2016). Pathways for energization of Ca in Mercury's exosphere. *Icarus*, *268*, 32–36. https://doi.org/10.1016/j.icarus.2015.12.035
Killen, R. M., Bida, T. A., & Morgan, T. H. (2005). The calcium exosphere of Mercury. *Icarus*, *173*(2), 300–311. https://doi.org/10.1016/j.icarus.2004.08.022
Killen, R. M., Burger, M. H., & Farrell, W. M. (2018). Exospheric escape: A parametrical study. *Advances in Space Research*, *62*(8), 2364–2371. https://doi.org/10.1016/j.asr.2017.06.015

Killen, R. M., Hurley, D. M., & Farrell, W. M. (2012). The effect on the lunar exosphere of a coronal mass ejection passage. *Journal of Geophysical Research*, *117*(E10), https://doi.org/10.1029/2011je004011
Killen, R. M., & Ip, W.-H. (1999). The surface-bounded atmosphere of Mercury and the Moon. *Reviews of Geophysics*, *37*(3), 361–406. https://doi.org/10.1029/1999rg900001
Killen, R. M., Morgan, T. H., Potter, A. E., Bacon, G., Ajang, I., & Poppe, A. R. (2021). Coronagraphic observations of the lunar sodium exosphere 2018 – 2019. *Icarus*, *355*, 114155. https://doi.org/10.1016/j.icarus.2020.114155
King, J. H., & Papitashvili, N. E. (2005). Solar wind spatial scales in and comparisons of hourly Wind and ACE plasma and magnetic field data. *Journal of Geophysical Research*, *110*(A2), A02104. https://doi.org/10.1029/2004ja010649
Leblanc, F., & Chaufray, J. Y. (2011). Mercury and moon He exospheres: Analysis and modeling. *Icarus*, *216*(2), 551–559. https://doi.org/10.1016/j.icarus.2011.09.028
Leblanc, F., Schmidt, C., Mangano, V., Mura, A., Cremonese, G., Raines, J. M., et al. (2022). Comparative Na and K Mercury and Moon exospheres. *Space Science Reviews*, *218*(2). https://doi.org/10.1007/s11214-022-00871-w
Lee, D.-W., Kim, S. J., Lee, D.-H., Jin, H., & Kim, K.-S. (2011). Three-dimensional simulations of the lunar sodium exosphere and its tail. *Journal of Geophysical Research*, *116*(A07213). https://doi.org/10.1029/2011ja016451
Li, S., & Milliken, R. E. (2017). Water on the surface of the Moon as seen by the Moon Mineralogy Mapper: Distribution, abundance, and origins. *Science Advances*, *3*(9). https://doi.org/10.1126/sciadv.1701471
Line, M. R., Mierkiewicz, E. J., Oliversen, R. J., Wilson, J. K., Haffner, L. M., & Roesler, F. L. (2012). Sodium atoms in the lunar exotail: Observed velocity and spatial distributions. *Icarus*, *219*(2), 609–617. https://doi.org/10.1016/j.icarus.2012.04.001
Liuzzo, L., Poppe, A. R., Halekas, J. S., Simon, S., & Cao, X. (2021). Investigating the Moon's interactions with the terrestrial magnetotail lobe plasma. *Geophysical Research Letters*, *48*(9). https://doi.org/10.1029/2021GL093566
Lue, C., Futaana, Y., Barabash, S., Wieser, M., Holmström, M., Bhardwaj, A., et al. (2011). Strong influence of lunar crustal fields on the solar wind flow. *Geophysical Research Letters*, *38*(3). https://doi.org/10.1029/2010gl046215
Lue, C., Halekas, J. S., Poppe, A. R., & McFadden, J. P. (2018). ARTEMIS observations of solar wind Proton scattering off the lunar surface. *Journal of Geophysical Research: Space Physics*, *123*(7), 5289–5299. https://doi.org/10.1029/2018JA025486
Mall, U., Kirsch, E., Cierpka, K., Wilken, B., Soding, A., Neubauer, F., et al. (1998). Direct observation of lunar pick-up ions near the Moon. *Geophysical Research Letters*, *25*(20), 3799–3802. https://doi.org/10.1029/1998gl900003
Manka, R. H., & Michel, F. C. (1970). Lunar atmosphere as a source of Argon-40 and other lunar surface elements. *Science*, *169*(3942), 278–280. https://doi.org/10.1126/science.169.3942.278
Matta, M., Smith, S., Baumgardner, J., Wilson, J., Martinis, C., & Mendillo, M. (2009). The sodium tail of the Moon. *Icarus*, *204*(2), 409–417. https://doi.org/10.1016/j.icarus.2009.06.017
McFadden, J. P., Carlson, C. W., Larson, D., Bonnell, J., Mozer, F., Angelopoulos, V., et al. (2008b). THEMIS ESA first Science results and performance issues. *Space Science Reviews*, *141*(1–4), 477–508. https://doi.org/10.1007/s11214-008-9433-1
McFadden, J. P., Carlson, C. W., Larson, D., Ludlam, M., Abiad, R., Elliott, B., et al. (2008). The THEMIS ESA plasma instrument and in-flight calibration. *Space Science Reviews*, *141*(1–4), 277–302. https://doi.org/10.1007/s11214-008-9440-2
McLain, J. L., Sprague, A. L., Grieves, G. A., Schriver, D., Travnicek, P., & Orlando, T. M. (2011). Electron-stimulated desorption of silicates: A potential source for ions in Mercury's space environment. *Journal of Geophysical Research*, *116*(E3), E03007. https://doi.org/10.1029/2010je003714
Mendillo, M., & Baumgardner, J. (1995). Constraints on the origin of the Moon's atmosphere from observations during a lunar eclipse. *Nature*, *377*(6548), 404–406. https://doi.org/10.1038/377404a0
Meyer, F. W., Harris, P. R., Taylor, C. N., Meyer, H. M., III, Barghouty, A. F., & Adams, J. H. (2011). Sputtering of lunar regolith simulant by protons and singly and multicharged Ar ions at solar wind energies. *Nuclear Instruments and Methods B*, *269*(11), 1316–1320. https://doi.org/10.1016/j.nimb.2010.11.091
Mierkiewicz, E. J., Line, M., Roesler, F. L., & Oliversen, R. J. (2006). Radial velocity observations of the extended lunar sodium tail. *Geophysical Research Letters*, *33*(20), L20106. https://doi.org/10.1029/2006GL027650
Morgan, T. H., & Killen, R. M. (1998). Production mechanisms for faint by possibly detectable coronae about asteroids. *Planetary and Space Science*, *46*(8), 843–850. https://doi.org/10.1016/s0032-0633(98)00029-4
Nénon, Q., & Poppe, A. R. (2021). Bombardment of lunar polar crater interiors by out-of-ecliptic ions: ARTEMIS observations. *The Planetary Science Journal*, *2*(116). https://doi.org/10.3847/PSJ/abfda2
Nishino, M. N., Harada, Y., Saito, Y., Tsunakawa, H., Takahashi, F., Yokota, S., et al. (2017). Kaguya observations of the lunar wake in the terrestrial foreshock: Surface potential change by bow-shock reflected ions. *Icarus*, *293*, 45–51. https://doi.org/10.1016/j.icarus.2017.04.005
Ong, L., Asphaug, E. I., Korycansky, D., & Coker, R. F. (2010). Volatile retention from cometary impacts on the Moon. *Icarus*, *207*(2), 578–589. https://doi.org/10.1016/j.icarus.2009.12.012
Pieters, C. M., Goswami, J. N., Clark, R. N., Annadurai, M., Boardman, J., Buratti, B., et al. (2009). Character and spatial distribution of OH/H_2O on the surface of the moon seen by M^3 on chandrayaan-1. *Science*, *326*(5952), 568–572. https://doi.org/10.1126/science.1178658
Pillinger, C. T., & Eglington, G. (1977). The chemistry of carbon in the lunar regolith. *Philosophical Transactions of the Royal Society A*, (1327), 285. https://doi.org/10.1098/rsta.1977.0076
Pillinger, C. T., Eglington, G., Gowar, A. P., & Jull, A. J. T. (1977). Carbon chemistry of the Luna 16 and 20 samples. *Philosophical Transactions of the Royal Society A*, (1319), 284. https://doi.org/10.1098/rsta.1977.0004
Pokorný, P., Janches, D., Sarantos, M., Szalay, J. R., Horányi, M., Nesvorný, D., & Kuchner, M. J. (2019). Meteoroids at the Moon: Orbital properties, surface vaporization, and impact Ejecta Production. *Journal of Geophysical Research: Planets*, *124*(3), 752–778. https://doi.org/10.1029/2018JE005912
Poppe, A. R., Farrell, W. M., & Halekas, J. S. (2018). Formation timescales of amorphous rims on lunar grains derived from ARTEMIS observations. *Journal of Geophysical Research: Planets*, *123*(1), 37–46. https://doi.org/10.1002/2017JE005426
Poppe, A. R., Halekas, J. S., & Harada, Y. (2022). Dataset for "A comprehensive model for pickup ion formation at the Moon". [Dataset]. https://doi.org/10.5281/zenodo.6994648
Poppe, A. R., Halekas, J. S., Lue, C., & Fatemi, S. (2017). ARTEMIS observations of the solar wind proton scattering function from lunar crustal magnetic anomalies. *Journal of Geophysical Research: Planets*, *122*(4), 771–783. https://doi.org/10.1002/2017je005313
Poppe, A. R., Halekas, J. S., Samad, R., Sarantos, M., & Delory, G. T. (2013). Model-based constraints on the lunar exosphere derived from ARTEMIS pick-up ion observations in the terrestrial magnetotail. *Journal of Geophysical Research*, *118*(5), 1–13. https://doi.org/10.1002/jgre.20090
Poppe, A. R., Halekas, J. S., Sarantos, M., & Delory, G. T. (2013). The self-sputtered contribution to the lunar exosphere. *Journal of Geophysical Research*, *118*(9), 1934–1944. https://doi.org/10.1002/jgre.20148

Poppe, A. R., Halekas, J. S., Szalay, J. R., Horányi, M., Levin, Z., & Kempf, S. (2016). LADEE/LDEX observations of lunar pickup ion distribution and variability. *Geophysical Research Letters*, *43*(7), 3069–3077. https://doi.org/10.1002/2016gl068393

Poppe, A. R., Samad, R., Halekas, J. S., Sarantos, M., Delory, G. T., Farrell, W. M., et al. (2012). ARTEMIS observations of lunar pick-up ions in the terrestrial magnetotail. *Geophysical Research Letters*, *39*(L17104). https://doi.org/10.1029/2012gl052909

Poppe, A. R., Sarantos, M., Halekas, J. S., Delory, G. T., Saito, Y., & Nishino, M. (2014). Anisotropic solar wind sputtering of the lunar surface induce by crustal magnetic anomalies. *Geophysical Research Letters*, *41*(14), 4865–4872. https://doi.org/10.1002/2014gl060523

Potter, A. E., Killen, R. M., & Morgan, T. H. (2000). Variation of lunar sodium during passage of the Moon through the Earth's magnetotail. *Journal of Geophysical Research*, *105*(E6), 15. https://doi.org/10.1029/1999je001213

Potter, A. E., & Morgan, T. H. (1988). Extended sodium exosphere of the Moon. *Geophysical Research Letters*, *15*(13), 1515–1518. https://doi.org/10.1029/gl015i013p01515

Potter, A. E., & Morgan, T. H. (1991). Observations of the lunar sodium exosphere. *Geophysical Research Letters*, *18*(11), 2089–2092. https://doi.org/10.1029/91gl02621

Potter, A. E., & Morgan, T. H. (1998). Coronagraphic observations of the lunar sodium exosphere near the lunar surface. *Journal of Geophysical Research*, *103*(E4), 8581–8586. https://doi.org/10.1029/98je00059

Prem, P., Artemieva, N. A., Goldstein, D. B., Varghese, P. L., & Trafton, L. M. (2015). Transport of water in a transient impact-generated lunar atmosphere. *Icarus*, *255*, 148–158. https://doi.org/10.1016/j.icarus.2014.10.017

Rottman, G. J. (1988). Observations of solar UV and EUV variability. *Advances in Space Research*, *8*(7), 53–66. https://doi.org/10.1016/0273-1177(88)90172-x

Saito, Y., Yokota, S., Asamura, K., Tanaka, T., Nishino, M. N., Yamamoto, T., et al. (2010). In-flight performance and initial results of plasma energy angle and composition experiment (PACE) on SELENE (Kaguya). *Space Science Reviews*, *154*, 265–303.

Saito, Y., Yokota, S., Tanaka, T., Asamura, K., Nishino, M. N., Fujimoto, M., et al. (2008). Solar wind proton reflection at the lunar surface: Low energy ion measurement by MAP-PACE onboard SELENE (KAGUYA). *Geophysical Research Letters*, *35*, L24205. https://doi.org/10.1029/2008GL036077

Sarantos, M., Hartle, R. E., Killen, R. M., Saito, Y., Slavin, J. A., & Glocer, A. (2012). Flux estimates of ions from the lunar exosphere. *Geophysical Research Letters*, *39*(L13101). https://doi.org/10.1029/2012gl052001

Sarantos, M., Killen, R. M., Glenar, D. A., Benna, M., & Stubbs, T. J. (2012). Metallic species, oxygen and silicon in the lunar exosphere: Upper limits and prospects for LADEE measurements. *Journal of Geophysical Research*, *117*(A03103). https://doi.org/10.1029/2011ja017044

Sarantos, M., Killen, R. M., Surjalal Sharma, A., & Slavin, J. A. (2008). Influence of plasma ions on source rates for the lunar exosphere during passage through the Earth's magnetosphere. *Geophysical Research Letters*, *35*(4), L04105. https://doi.org/10.1029/2007gl032310

Sarantos, M., & Tsavachidis, S. (2020). The boundary of Alkali surface boundary Exospheres of Mercury and the Moon. *Geophysical Research Letters*, *47*(16). https://doi.org/10.1029/2020GL088930

Sarantos, M., & Tsavachidis, S. (2021). Lags in desorption of lunar volatiles. *The Astrophysical Journal Letters*, *919*(L14). https://doi.org/10.3847/2041-8213/ac205b

Schorghofer, N. (2014). Migration calculations for water in the exosphere of the Moon: Dusk-dawn asymmetry, heterogeneous trapping, and D/H fractionation. *Geophysical Research Letters*, *41*(14), 4888–4893. https://doi.org/10.1002/2014GL060820

Schorghofer, N. (2015). Two-dimensional description of surface-bounded exospheres with application to the migration of water molecules on the Moon. *Physical Review E - Statistical Physics, Plasmas, Fluids, and Related Interdisciplinary Topics*, *91*(5), 052154. https://doi.org/10.1103/PhysRevE.91.052154

Schörghofer, N., Benna, M., Berezhnoy, A. A., Greenhagen, B., Jones, B. M., Li, S., et al. (2021). Water group Exospheres and surface interactions on the Moon, Mercury, and Ceres. *Space Science Reviews*, *217*(74). https://doi.org/10.1007/s11214-021-00846-3

Schorghofer, N., Lucey, P., & Williams, J.-P. (2017). Theoretical time variability of mobile water on the Moon and its geographic pattern. *Icarus*, *298*, 111–116. https://doi.org/10.1016/j.icarus.2017.01.029

Sigmund, P. (1969). Theory of sputtering. I. Sputtering yield of amorphous and polycrystalline targets. *Physics Reviews*, *184*(2), 383–416. https://doi.org/10.1103/physrev.187.768

Smith, S. M., Wilson, J. K., Baumgardner, J., & Mendillo, M. (1999). Discovery of the distant lunar sodium tail and its enhancement following the Leonid meteor shower of 1998. *Geophysical Research Letters*, *26*(12), 1649–1652. https://doi.org/10.1029/1999gl900314

Smyth, W. H., & Marconi, M. L. (1995). Theoretical overview and modeling of the sodium and potassium atmospheres of the Moon. *The Astrophysical Journal*, *443*, 371–392. https://doi.org/10.1086/175532

Stern, S. A., Cook, J. C., Chaufray, J.-Y., Feldman, P. D., Gladstone, G. R., & Retherford, K. D. (2013). Lunar atmospheric H_2 detections by the LAMP UV spectrograph on the lunar reconnaissance orbiter. *Icarus*, *226*(2), 1210–1213. https://doi.org/10.1016/j.icarus.2013.07.011

Stern, S. A., Parker, J. W., Morgan, T. H., Flynn, B. C., Hunten, D. M., Sprague, A. L., et al. (1997). An HST search for magnesium in the lunar atmosphere. *Icarus*, *127*(2), 523–526. https://doi.org/10.1006/icar.1997.5716

Stewart, B. D., Pierazzo, E., Goldstein, D. B., Varghese, P. L., & Trafton, L. M. (2011). Simulations of a comet impact on the Moon and associated ice deposition in polar cold traps. *Icarus*, *215*, 1–16. https://doi.org/10.1016/j.icarus.2011.03.014

Sunshine, J. M., Farnham, T. L., Feaga, L. M., Groussin, O., Merlin, F., Millikan, R. E., & A'Hearn, M. F. (2009). Temporal and spatial variability of lunar hydration as observed by the deep impact spacecraft. *Science*, *326*(5952), 565–568. https://doi.org/10.1126/science.1179788

Szabo, P. S., Biber, H., Jäggi, N., Brenner, M., Weichselbaum, D., Niggas, A., et al. (2020). Dynamic potential sputtering of lunar analog material by solar wind ions. *The Astrophysical Journal*, *891*(100). https://doi.org/10.3847/1538-4357/ab7008

Szabo, P. S., Chiba, R., Biber, H., Stadlmeyer, R., Berger, B. M., Mayer, D., et al. (2018). Solar wind sputtering of wollastonite as a lunar analogue material – Comparisons between experiments and simulations. *Icarus*, *314*, 98–105. https://doi.org/10.1016/j.icarus.2018.05.028

Szalay, J. R., & Horányi, M. (2015). Annual variation and synodic modulation of the sporadic meteoroid flux to the Moon. *Geophysical Research Letters*, *42*(24), 10580–10584. https://doi.org/10.1002/2015gl066908

Szalay, J. R., Horányi, M., Colaprete, A., & Sarantos, M. (2016). Meteoritic influence on sodium and potassium abundance in the lunar exosphere measured by LADEE. *Geophysical Research Letters*, *43*(12), 6096–6102. https://doi.org/10.1002/2016gl069541

Tanaka, T., Saito, Y., Yokota, S., Asamura, K., Nishino, M. N., Tsunakawa, H., et al. (2009). First in situ observation of the Moon-originating ions in the Earth's Magnetosphere by MAP-PACE on SELENE (KAGUYA). *Geophysical Research Letters*, *36*(22), L22106. https://doi.org/10.1029/2009gl040682

Thampi, S. V., Sridharan, R., Das, T. P., Ahmed, S. M., Kamalakar, J. A., & Bhardwaj, A. (2015). The spatial distribution of molecular hydrogen in the lunar atmosphere – New results. *Planetary and Space Science*, *106*, 142–147. https://doi.org/10.1016/j.pss.2014.12.018

Thompson, M. W., Farmery, B. W., & Newson, P. A. (1968). A mechanical spectrometer for analyzing the energy distribution of sputtered atoms of copper and gold. *Philosophical Magazine A*, *18*(152), 361–383. https://doi.org/10.1080/14786436808227357

Tucker, O. J., Farrell, W. M., Killen, R. M., & Hurley, D. M. (2019). Solar wind implantation into the lunar regolith: Monte Carlo simulations of H retention in a surface with defects and the H_2 exosphere. *Journal of Geophysical Research: Planets*, *124*(2), 278–293. https://doi.org/10.1029/2018JE005805

Valiev, R. R., Berezhnoy, A. A., Gritsenko, I. S., Merzlikin, B. S., Cherepanov, V. N., Kurten, T., & Wöhler, C. (2020). Photolysis of diatomic molecules as a source of atoms in planetary exospheres. *Astronomy and Astrophysics*, *633*(A39). https://doi.org/10.1051/0004-6361/201936230

Verani, S., Barbieri, C., Benn, C., & Cremonese, G. (1998). Possible detection of meteor stream effects on the lunar sodium atmosphere. *Planetary and Space Science*, *46*(8), 1003–1006. https://doi.org/10.1016/s0032-0633(98)00024-5

Vorburger, A., Wurz, P., Barabash, S., Wieser, M., Futaana, Y., Holmström, M., et al. (2012). Energetic neutral atom observations of magnetic anomalies on the lunar surface. *Journal of Geophysical Research*, *117*(A7). https://doi.org/10.1029/2012ja017553

Vorburger, A., Wurz, P., Barabash, S., Wieser, M., Futaana, Y., Holmström, M., et al. (2014). First direct observation of sputtered lunar oxygen. *Journal of Geophysical Research*, *119*(2), 709–722. https://doi.org/10.1002/2013JA019207

Wang, J., Wu, C., Qiu, Y. L., Meng, X. M., Cai, H. B., Cao, L., et al. (2015). An unprecedented constraint on water content in the sunlit lunar exosphere seen by Lunar-based Ultraviolet Telescope of Chang'E-3 mission. *Planetary and Space Science*, *109–110*, 123–128. https://doi.org/10.1016/j.pss.2015.02.006

Wang, X.-D., Zong, Q. G., Wang, J. S., Cui, J., Reme, H., Dandouras, I., et al. (2011). Detection of m/q=2 pickup ions in the plasma environment of the Moon: The trace of exospheric. *Geophysical Research Letters*, *38*(L14204). https://doi.org/10.1029/2011gl047488

Weygand, J. M., Ipavich, F. M., Wurz, P., Paquette, J. A., & Bochsler, P. (2001). Determination of the $^{36}Ar/^{38}Ar$ isotopic abundance ratio of the solar wind using SOHO/CELIAS/MTOF. *Geochimica et Cosmochimica Acta*, *65*(24), 4589–4596. https://doi.org/10.1016/S0016-7037(01)00740-2

Wilson, J. K., Baumgardner, J., & Mendillo, M. (2003). The outer limits of the lunar sodium exosphere. *Geophysical Research Letters*, *30*(12). https://doi.org/10.1029/2003GL017443

Wilson, J. K., Mendillo, M., & Spence, H. E. (2006). Magnetospheric influence on the Moon's exosphere. *Journal of Geophysical Research*, *111*(A7), A07207. https://doi.org/10.1029/2005ja011364

Woods, T. N., Eparvier, F. G., Fontenla, J., Harder, J., Kopp, G., McClintock, W. E., et al. (2004). Solar irradiation variability during the October 2003 solar storm period. *Geophysical Research Letters*, *31*(10), L10802. https://doi.org/10.1029/2004GL019571

Woods, T. N., Hock, R., Eparvier, F., Jones, A. R., Chamberlin, P. C., Klimchuk, J. A., et al. (2011). New solar extreme-ultraviolet irradiance observations during flares. *The Astrophysical Journal*, *739*(59). https://doi.org/10.1088/0004-637X/739/2/59

Wurz, P., Fatemi, S., Galli, A., Halekas, J., Harada, Y., Jäggi, N., et al. (2022). Particles and photons as drivers for particle release from the surfaces of the Moon and Mercury. *Space Science Reviews*, *218*(10). https://doi.org/10.1007/s11214-022-00875-6

Wurz, P., Rohner, U., Whitby, J. A., Kolb, C., Lammer, H., Dobnikar, P., & Martín-Fernández, J. A. (2007). The lunar exosphere: The sputtering contribution. *Icarus*, *191*(2), 486–496. https://doi.org/10.1016/j.icarus.2007.04.034

Xu, S., Poppe, A. R., Halekas, J. S., Mitchell, D. L., McFadden, J. P., & Harada, Y. (2019). Mapping the lunar wake Potential structure with ARTEMIS data. *Journal of Geophysical Research: Space Physics*, *124*(5), 3360–3377. https://doi.org/10.1029/2019JA026536

Yakshinskiy, B. V., & Madey, T. E. (1999). Photon-stimulated desorption as a substantial source of sodium in the lunar atmosphere. *Nature*, *400*(6745), 642–644. https://doi.org/10.1038/23204

Yakshinskiy, B. V., & Madey, T. E. (2004). Photon-stimulated desorption of Na from a lunar sample: Temperature-dependent effects. *Icarus*, *168*(1), 53–59. https://doi.org/10.1016/j.icarus.2003.12.007

Yokota, S., Saito, Y., Asamura, K., Nishino, M. N., Yamamoto, T. I., Tsunakawa, H., et al. (2014). Kaguya observation of the ion acceleration around a lunar crustal magnetic anomaly. *Planetary and Space Science*, *93–94*, 87–95. https://doi.org/10.1016/j.pss.2014.02.007

Yokota, S., Saito, Y., Asamura, K., Tanaka, T., Nishino, M. N., Tsunakawa, H., et al. (2009). First direct detection of ions originating from the Moon by MAP-PACE IMA onboard SELENE (KAGUYA). *Geophysical Research Letters*, *36*, L11201. https://doi.org/10.1029/2009gl038185

Yokota, S., Tanaka, T., Saito, Y., Asamura, K., Nishino, M. N., Fujimoto, M., et al. (2014). Structure of the ionized lunar sodium and potassium exosphere: Dawn-dusk asymmetry. *Journal of Geophysical Research: Planets*, *119*(4), 798–809. https://doi.org/10.1002/2013je004529

Yokota, S., Terada, K., Saito, Y., Kato, D., Asamura, K., Nishino, M. N., et al. (2020). KAGUYA observation of global emissions of indigenous carbon ions from the Moon. *Science Advances*, *6*(19). https://doi.org/10.1126/sciadv.aba1050

Zhang, H., Khurana, K. K., Kivelson, M. G., Angelopoulos, V., Wan, W. X., Liu, L. B., et al. (2014). Three-dimensional lunar wake reconstructed from ARTEMIS data. *Journal of Geophysical Research: Space Physics*, *119*(7), 5220–5243. https://doi.org/10.1002/2014JA020111

Zhou, X.-Z., Angelopoulos, V., Poppe, A. R., & Halekas, J. S. (2013). ARTEMIS observations of lunar pickup ions: Mass constraints on ion species. *Journal of Geophysical Research*, *118*(9), 1766–1774. https://doi.org/10.1002/jgre.20125

Zhou, X.-Z., Angelopoulos, V., Poppe, A. R., Halekas, J. S., Khurana, K. K., Kivelson, M. G., et al. (2014). Lunar dayside current in the terrestrial lobe: ARTEMIS observations. *Journal of Geophysical Research: Space Physics*, *119*(5), 3381–3391. https://doi.org/10.1002/2014JA019842